8-2017

Piezoelectric bistable buckled beam energy harvester.

Brian Edward Allgeier
University of Louisville

PIEZOELECTRIC BISTABLE BUCKLED BEAM ENERGY HARVESTER

By

Brian Edward Allgeier
B.S. Physics, University of Kentucky, 2016
B.S. Mathematics, University of Kentucky, 2016

A Thesis
Submitted to the Faculty of the
University of Louisville
J.B. Speed School of Engineering
as Partial Fulfillment of the Requirements
for the Professional Degree

Master of Science in Mechanical Engineering

Department of Mechanical Engineering
University of Louisville
Louisville, Kentucky

August 2017

PIEZOELECTRIC BISTABLE BUCKLED BEAM ENERGY HARVESTER

Submitted by: _____
Brian Edward Allgeier

A Thesis Approved On

July 12, 2017

by the Following Examination Committee:

_____
Thomas Berfield, Thesis Director

_____
Christopher Richards

_____
Shamus McNamara

ACKNOWLEDGMENTS

A great deal of thanks to Dr. Tom Berfield, for the opportunity and guidance.
And additional thanks to Jerry and Sue Allgeier, for the support and interest;
to Wimmer, for the continuously enduring empathetic jadedness;
to Katie, for helping keep me sane through the year—
or at least choosing to be insane with me.

ABSTRACT

PIEZOELECTRIC BISTABLE BUCKLED BEAM ENERGY HARVESTER

Brian Edward Allgeier

July 12, 2017

A novel energy harvesting device design is presented to be created via microfabrication techniques. Such devices have countless applications for powering low-current electrical devices, especially wireless sensors or transmitters. This microelectromechanical system (MEMS) design utilizes the piezoelectric response of a bistable buckled beam to gather electrical energy via ambient vibrations. While many traditional piezoelectric energy harvesters (PEH) consist of simple cantilever beam geometries, this nonlinear design utilizes inertial effects of torsional lever arms to actuate a central buckled beam to snap between its two stable states; such an abrupt strain on the piezoelectric beam potentially produces a significantly increased electrical response over a wider range of excitation frequencies than is possible with simpler linear systems. The geometries of all structural layers of the device are described in detail, in addition to the cleanroom processes needed to create each MEMS device layer. Experimental fabrication process steps and results, performed by the author's work in the University of Louisville's Micro-Nano Technology Center, are described in detail. The most successful, complete microfabrication process flow is given to the best of the author's abilities. Potential improvements and ideas for future work are given in conclusion.

TABLE OF CONTENTS

LIST OF FIGURES

I. INTRODUCTION

A. Overview of Work Presented

The purpose of this thesis is to introduce an energy harvester design targeted to prove useful in a wide variety of low-power electrical applications. The design of the device will be implemented via modern microfabrication techniques and its performance analyzed and compared to those of more traditional harvester designs.

The first chapter begins by familiarizing the reader with common microfabrication processes, namely photolithography and surface- and micro-machining, while further explaining their uses in traditional micro-electromechanical systems (MEMS). A broad overview of the piezoelectric energy harvester (PEH) design of this text is explained next, in addition to potential advantages over previous PEH designs. The wide range of applications of such harvesters is discussed, especially their use in underground water line sensors and wireless transmitters.

The second chapter contains an insight into previous publications regarding MEMS harvesters. A quick overview of basic vibrational energy harvesting theory is given, grounded in the equations of previous literature. Traditional piezoelectric energy harvesters, such as simple cantilever beam harvesters, are described, including their performance and fabrication processes. Research on various piezoelectric material depositions and properties, namely that of aluminum nitride, is given in light of similar work performed by the author to be described later in the text.

The third chapter contains the details of the device design geometry and of all the device cells which appear on the lithography photomasks utilized by this research,

beginning with the theoretical structure of the device (to be created via microfabrication processes) and intended operation. The exact geometry and functionality of each structural layer of the simplest version of the device is given and explained in terms of L-Edit software photomask layouts and descriptions of the layer materials. Other more complicated device designs—denoted the auxiliary designs—are explored as well, in addition to traditional cantilever designs and simple buckled beam structures. The results of software simulations of the KOH anisotropic release etch step are given, and the consequences of these results are explored in terms of device fabrication and functionality.

The fourth chapter contains information on the experimental fabrication of the device, starting with an overview of the University of Louisville's Micro-Nano Technology Center cleanroom facility, where virtually all fabrication procedures of this research have taken place. The following four sections of the chapter describe in detail the materials comprising each structural device layer and the processes used to deposit each material: silicon dioxide, deposited onto blank silicon wafers via thermal oxide chamber; stressed silicon nitride, deposited via pulsed plasma-enhanced chemical vapor deposition; metal electrodes via physical vapor deposition; and aluminum nitride piezoelectric material, deposited via a heated physical vapor deposition combined with a nitrogen gas mixture. The next three sections of the chapter describe the exact details of the following important microfabrication procedures: photolithography technique and photoresist and development recipes; dry etching recipes for each structural surface layer; technique for anisotropic wet etching through the silicon substrate and the final release steps used to free the major components of the device. This chapter concludes with a complete process overview, which serves to bring any future researchers up to successful fabrication as quickly and easily as possible.

The fifth chapter describes the experimental testing of the performance of completed devices, especially their energy harvesting abilities in terms of current genera-

tion and response to a range of driving frequencies and amplitudes. An explanation of the experimental testing procedure is given, and a summary and analysis of the data is performed, with the final results given in conclusion.

The sixth and final chapter begins with comparisons between the performance of the energy harvester of this thesis (as summarized in the previous section) and that of traditional cantilever beam harvester designs, as summarized in previous literature. Possible improvements, changes, and ideas for future work are suggested for following researchers hoping to continue the research provided in this thesis.

B. MEMS Piezoelectric Energy Harvesting

Piezoelectric energy harvesting is not an especially novel idea; the premise of gathering usable energy via the otherwise wasted vibrational movement of surrounding media has been sought after for years. However, the design and fabrication of new and improved harvesting devices is a continued and ongoing subject of microfabrication research today. The topic of this thesis is the research and development of an original MEMS PEH design, especially regarding the details of the unique bistable buckled beam geometry and the process of experimental fabrication utilizing the microfabrication facilities offered by University of Louisville's Micro-Nano Technology Center (MNTC).

MEMS devices in general are traditionally built as a series of material layers deposited and patterned atop the polished surface of a crystalline silicon wafer. Each material layer, typically ranging in thickness from tens of nanometers (nm) to tens of micrometers (microns, μm), serves a dedicated purpose—whether that be as a sacrificial or protective layer for future processes, or as a structural layer for the completed device. Each layer deposition (performed via a number of processes such as physical vapor deposition, chemical vapor deposition, spinning, evaporation, among others) can be patterned to a specific geometry through the well-developed process

of photolithography: First, a thin layer of a UV-sensitive photoresist is deposited (usually via spinning) on top of the unpatterned layer. A patterned photomask then allows UV light from a mask-alignment machine to pass through only to the regions in the photomask layer where the underneath material is undesired. The UV light induces changes within the molecular bonds of the photoresist such that it will be easily dissolved via a developing agent, while the unexposed regions remain (for positive photoresists—the converse is true for negative photoresists). At this point, the underlying, undesired material regions are exposed and can be etched away by a number of various methods (such as physical ion etching, reactive ion etching, deep reactive ion etching, wet chemical etching, among others); these methods are chosen so that they selectively etch the undesired material at a considerably higher rate than the other present materials (such as the hardened photoresist). Once the excess photoresist is removed, the wafer sample is left with a patterned topmost layer of the original material.

Utilizing this process of repeated deposition, patterning, and etching, MEMS devices can quickly be built via several stacked layers of patterned materials. The term *surface micromachining* is used to describe a process which consists solely of stacking these thin layers atop the surface of the supporting wafer to create a device. However, while surface micromachining serves a great purpose especially for applications in integrated circuitry and transistor fabrication, it is sometimes insufficient for other applications; for example, devices which require physical freedom of movement—a property often desired in MEMS devices (or other mechanical facets, such as microfluidic channels)—would most likely require a *bulk micromachining* process in which the supporting silicon wafer itself is patterned and etched to specified requirements. Some applications may call for only partial etching of holes or trenches within the bulk silicon, while others may require removal of the entire thickness of the wafer in certain locations of the sample in question (as is the case for this device).

Most—if not, all—PEH designs necessitate the use of both surface and bulk micromachining. The key component to any MEMS PEH is the piezoelectric material layer: such a material generates a small, yet significant voltage in response to induced strains within the material—a crucial phenomenon for converting vibrational motion into electrical energy. Many PEH designs utilize the use of one or more proof masses attached to a central beam structure (to which the piezelectric material is adhered) in order to induce oscillatory motion in the beam and induce strain within the piezoelectric layer when the device is placed in a vibrating ambient environment. In order for the response voltages to be of any use, however, bottom and top metal electrodes must be adhered to the corresponding faces of the piezoelectric material layer to allow an obtainable current to be generated and subsequently harvested. This electrode-piezoelectric-electrode pattern of layers will be referred to as the *piezoelectric stack* for the remainder of this text. This piezoelectric stack comprises the major components of the PEH and is created via the surface micromachining techniques described in general above. One or more structural layers may be required in addition for added rigidity and strength to the device.

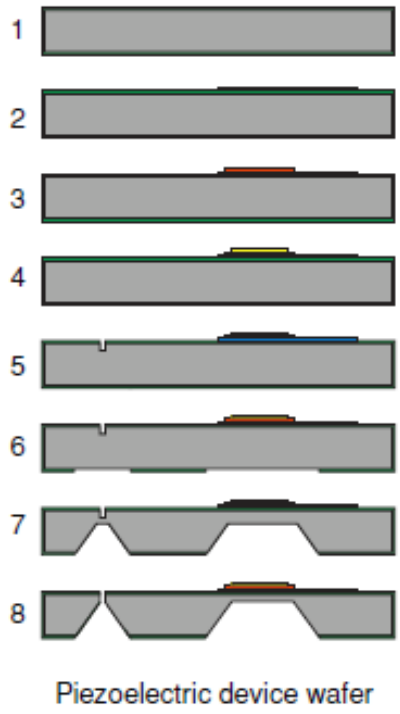

FIGURE 1: The process flow of a simple cantilever PEH: beginning with an oxide or nitride protection layer (1), a piezoelectric layer (3) is deposited onto a bottom electrode (2) and then covered with a top electrode (4). The PEH geometry is formed after patterning the backside protective layer and controlled bulk micromachining (5-7); a final release step (8) frees the structure. [1]

However, since a piezoelectric-based harvester requires, by definition, strain in order to operate—and thus physical movement—the piezoelectric stack must be freed from the surface onto which it is adhered during its deposition. Bulk micromachining from the backside (the op-

posite face on which surface micromachining takes place) allows for this important release step. Figure 1 outlines the process flow of a traditional cantilever beam PEH: the first half of the process flow consists of the deposition of the piezoelectric stack onto the surface, beginning with the bottom electrode and ending with the top electrode; the second half of the process entails bulk etching through the backside of the wafer to achieve the desired geometry and finally releasing the structure to move freely. A very similar process is used to create the harvesting device of this research; the major difference lies not specifically within the processing flow used to create the harvester, but very heavily within the geometry of the material layers of the device (and the material properties of these layers). It is the geometry of the device which most greatly influences its function, as described in the following section.

C. Bistable Buckled Beam Structure

Perhaps the simplest—and most traditional—PEH since the beginning of MEMS technology has been the cantilever harvester design: a thin cantilever beam structure (containing a piezoelectric film)—perhaps with a proof mass attached to the end of the beam—oscillates back and forth in response to forced ambient vibrations. The continuously-changing bending moment of the beam is then responsible for resulting current generation.

In a bistable buckled beam design (represented in a macroscale variation in Figure 2), the main beam is not cantilevered but is rather anchored on both ends. The structural material of the beam (here, a silicon nitride film) is compressively stressed so that the beam will naturally buckle slightly under its own compression. Further, the beam is anchored on either side by thin pivot arms exactly halfway along the length of the beam; this central anchor forces a nodal point in the buckled beam state. The resulting beam shape, as viewed from a side profile, roughly resembles a sinusoidal wave (albeit with zero-slope boundary conditions) comprising exactly one

wavelength between the two ends of the beam. Thus, the main beam will naturally exist in one of only two lowest energy states (say, to extend the analogy, one state corresponding to a positive sine wave and the other to a negative sine wave). Hence, the term *bistable* is used to describe such a buckled beam.

A bistable buckled beam as described above will not—by itself—respond in any very significant way to ambient vibrations (in the direction normal to the main face of the beam, *i.e.* parallel to the direction of the beam's bending). In order to induce strain onto the beam, some sort of inertial proof masses are necessary. In this design, two proof masses are attached to the ends of lever arms anchored to the two pivot arms at the central node on either side of the main beam. Under forced vibrations, these lever arms—acting like simple cantilever beams themselves—oscillate up and down and exert torques onto the pivot arms of the beam; in theory, these torques will be great enough to snap the buckled beam from one stable state to the other stable state, acting in phase with the motion of the proof masses and the ambient vibrations.

This bistable buckled beam geometry is illustrated in Figure 2 by a large-scale model, specifically showing each of the two stable states. In the top image (Beam State 1), the lever arms and proof masses are in the upward position and the beam shape forms a negative sine wave from this specific side view; in the bottom image (Beam State 2), the lever arms and proof masses point downward and the beam forms a positive sine wave shape. When the beam oscillates vertically with respect to the proof masses (as is the case under a forced vibration), the lever arms will torque the beam from one state to the other. This snapping between stable states is the key difference between this device and traditional cantilever designs. It is hypothesized that the extremely abrupt snapping motion of the piezoelectric beam produces a greater piezoelectric current than the more continuous, gentle swaying motion of a traditional design. A larger induced current allows for greater amount of electrical

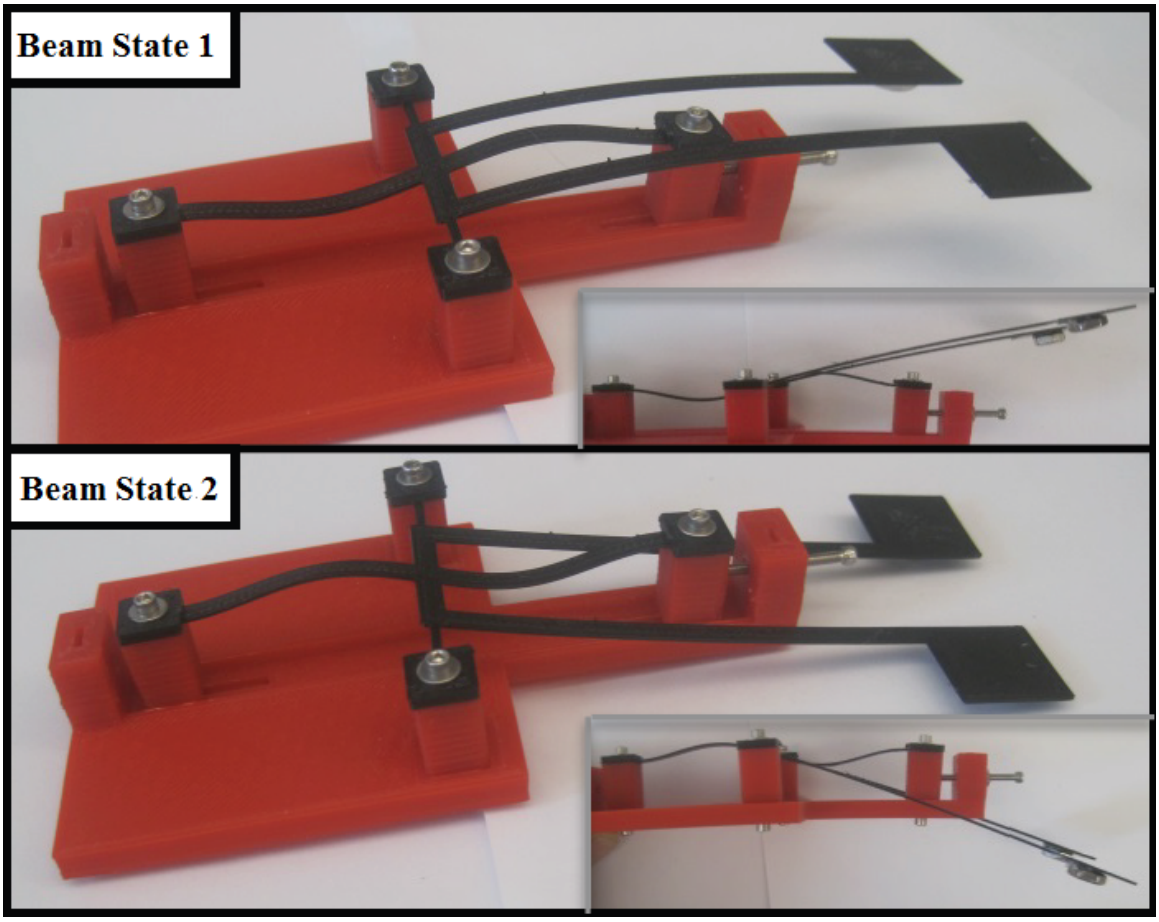

FIGURE 2: A macroscale model of the bistable buckled beam harvester design. The two separate images (top and bottom) correlate to the two stable states of the harvester beam.

energy to be harvested and thus for significantly increased efficiency and a wider range of applications for which the MEMS PEH could provide power.

D. Potential Applications

Functional MEMS vibrational energy harvesters would prove useful in many low-power applications. Perhaps the most likely application would be powering small transmitters for, say, the wireless transfer of collected data via various sensors. Small sensors placed in fairly permanent locations could prove difficult or highly inconvenient to constantly maintain sufficient power for gathering or sending data, either by wired connections or via regular maintenance. Thus, some form of small renewable

power source is much desired. Many popular forms of renewable energy—such as solar—would most likely become far too expensive for the small amount of electrical energy needed. Thus, a smaller, cheaper source of power is desired, such as a MEMS PEH.

For example, pressure sensors, stress sensors, strain gauges, and fluid flow sensors all have applications in underground pipelines. Such an environment could present an ideal application for a PEH; if the pipe were active and significant water flow occurs for significant periods of time, the pipe may vibrate at large enough amplitudes to allow for energy harvesting via a PEH. This gathered electrical energy could power a transmitter to send the sensed data to an above-ground receiver, without need for lead wires to an external power supply or regular maintenance and battery changing. Ideally, the entire system could operate successfully and independently for a significant amount of time, thus minimizing the need for timely and costly underground labor, pipeline checkup, maintenance routines.

PEH applications extend far beyond underground waterlines; as renewable energy sources become increasingly important, MEMS harvesters may perhaps take a substantial place in powering a wide range of low-power applications where other energy sources may be inefficient in design, cost-effectiveness, or dependability. The purpose of this thesis is to advance the progress of research on a novel design of PEH towards the ultimate goal of increasing applicability of MEMS harvesters for use in modern sensors, transmitters, and other low-power electrical devices.

II. LITERATURE REVIEW

A. Linear Vibrational Energy Harvesting Theory

Vibrational energy harvesting theory for linear systems is firmly rooted in the equations of linear mechanical vibrations, a topic that has been thoroughly explored and understood to a great depth for quite some time. The simplest descriptions of vibrational energy harvesting can be based on the forced single degree of freedom archetype problem of vibrations theory. (Significantly more in-depth analyses of energy harvesting via ambient vibrational sources for various harvesting devices can be found in [2–4]) As explained in [2], the equation of motion is given by

$$m\ddot{x} + c\dot{x} + kx = F\sin(\omega t). \tag{1}$$

where x denotes the displacement of mass m under spring stiffness k and a damping factor of c. An outside driving force of amplitude F and frequency ω is the ambient source of the harvested energy; meanwhile, the system's damping factor accounts for the dissipation of energy during oscillation. The magnitude of the instantaneous power associated with each of these mechanisms is limited by this energy dissipation—and thus the damping factor—and is given simply by $c\dot{x}^2$. The general steady-state solution to this system is

$$x(t) = \frac{F\sin\left[\omega t - \arctan\left(c\omega/(k-\omega^2 m)\right)\right]}{\sqrt{(k-\omega^2 m)^2 + c^2\omega^2}}, \tag{2}$$

and so the instantaneous power can be integrated over a single period $\tau = 2\pi/\omega$ to find the maximal harvestable energy per cycle:

$$E_{\text{cycle}} = \frac{\pi c \omega F^2}{(k - \omega^2 m)^2 + c^2 \omega^2}. \tag{3}$$

A related useful quantity is the average power output, given by E_{cycle}/τ:

$$P_{\text{average}} = \frac{c \omega^2 F^2}{2\left[(k - \omega^2 m)^2 + c^2 \omega^2\right]}. \tag{4}$$

Thus, for the simplest single degree of freedom vibration problem, the optimal harvestable energy and the average produceable power is easily calculable. Simple linear vibrational energy harvesters based on the movement of proof masses—say, at the end of cantilever piezoelectric beam—can be modeled by such a single degree of freedom system, where the displacement of the mass is the degree of freedom. The proof mass—or the *equivalent* mass of complicated geometries—takes the place of the system inertia m; the geometry, material composition, and piezoelectric properties of the harvester beam are the major factors responsible for the system equivalent stiffness k and the equivalent damping c, the latter of which directly determines the amount of produceable power. Such values could hypothetically be calculated via careful analysis of the beam—most likely via a finite elements model—or via direct experimental measurement.

This theory of mechanical vibrations extends beautifully beyond the one degree of freedom regimes as well: multiple degree of freedom linear systems are described by an analogous matrix form of Eq. 1, while continuous linear systems are modeled by similar Sturm-Liouville equations (where functions and operators take the place of vectors and matrices). Thus, linear harvesting with multiple degrees of freedom is mathematically describable, although such work does not appear in this text since the focus of this research is a single degree of freedom system.

However, it is very important to note that the above theory is limited to the description of *linear* systems—that is, those governed by linear equations of motion such as Eq. 1. Buckled beams, such as those employed in the design of this research, are *non*linear systems and thus are not adequately described by linear equations of motion. To illustrate, a point on a buckled beam, when perturbed by an oscillatory driving force, will not typically exhibit a simple harmonic displacement in response; instead, the displacement of the point is determined by the nature of the snap-through behavior of the buckled beam and will most likely be much less smooth than that of simple harmonic motion.

Mathematical descriptions of these nonlinear systems are much more complicated to derive and are quite susceptible to great inaccuracies which arise due to very small initial errors in modeling (due to the "chaotic" behavior of the nonlinear dynamics of the system). For this reason, mathematical models of the proposed device will not be explored further (although mathematical descriptions of bistable buckled beam geometries can be found in [7] and [8] and further studies of other buckled structures in [9] and [10], while several useful results of these texts are cited in the following sections). In the case of this thesis, measured piezoelectric response of the nonlinear harvester design—as a result of microfabrication and experimentation—will be of major interest.

B. Traditional Linear Systems

There have been a wide variety of harvester geometries explored in the literature over the past few decades. While linear, cantilever-based systems have always been a topic of interest in the energy-harvesting community, more complicated geometries with nonlinear characteristics have been continuing to emerge and improve upon previous designs.

A cantilever beam "archetype" system is perhaps the simplest linear harvesting geometry in terms of modeling and fabricating. An example of such a system is described in [4], [11] and illustrated in Figure 3 from the latter. This specific harvester geometry comprises a cantilever beam 11 mm in length and an oversized tungsten proof mass of size $17 \times 7.7 \times 3.6$ mm. The main beam is composed of two PZT piezoelectric layers of 0.28 mm thickness stacked against a middle brass electrode 0.1 mm thick. At a frequency of 120 Hz (the approximate resonant frequency of the beam), the harvester was reported to produce a peak electrical power of about 375 μW; this output was enough to power a radio frequency transceiver, one of the most likely and useful applications for MEMS PEHs.

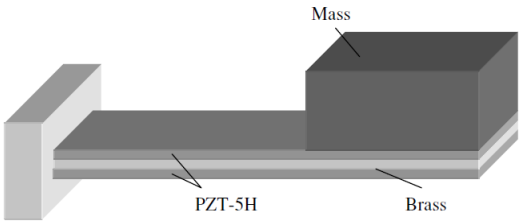

FIGURE 3: A simple cantilever beam consisting of two PZT piezoelectric layers stacked against a brass electrode and a large proof mass loaded at the end of the beam. [11]

Via the work described above, it was concluded in [4], [11] that the output power produceable by a cantilever harvester is proportional to the end-loaded proof mass. Of course, this conclusion makes intuitive sense since it is the proof mass which drives the strain of the beam during oscillation. Thus, a more powerful energy-harvesting geometry is one which allows for a larger proof mass without sacrificing beam integrity or piezoelectric performance of the beam material.

However, although sufficient power outputs have been proven to be produceable by simple cantilever harvesters, these peak outputs are able to occur only within a relatively small range of excitation frequencies centered about the resonant frequency of the beam (illustrated in the next section). Such a trait is characteristic of any linear system under an oscillatory forced vibration. It is hypothesized that nonlinear systems—say, via a bistable buckling geometry—will provide similar or improved power performance at a wider range of excitation frequencies.

C. Bistable Nonlinear Systems

While narrow bandwidths and high resonant frequencies plague the practicality of most small-scale cantilever harvester designs, more complicated nonlinear systems may provide a more applicable solution.

One such nonlinear adaptation to the cantilever beam harvester is illustrated in Figure 4; this design [12] utilizes magnetic repulsion between permanent magnets located at the end of the beam and directly across from the beam equilibrium point. This magnetic coupling, responsible for the system's nonlinearity, enhances the beam's response and sensitivity over a wider range of frequencies by increasing the amplitude of the beam deflection via the added repulsion. Observation of this effect over a range of frequencies can be interpreted through the response voltage of the piezoelectric beam; the gathered data is displayed in Figure 5 (left image, solid line), as compared to the corresponding response of the same beam with the opposing magnet removed, returning the system to a linear behavior (left image, dashed line).

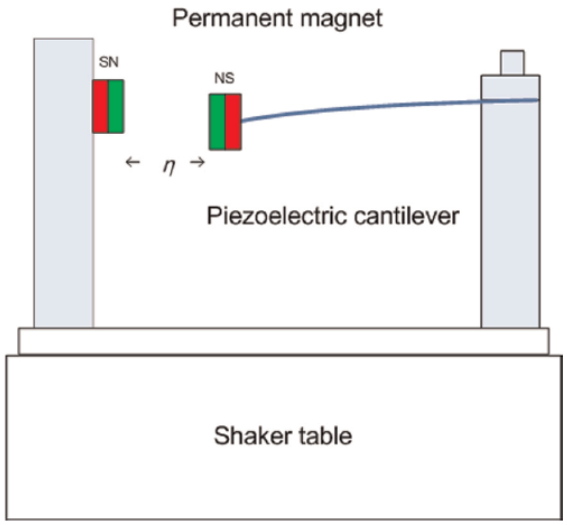

FIGURE 4: A nonlinear harvester adapted from a simple cantilever beam which utilizies magnetic coupling to enhance response voltage amplitude over a larger bandwidth. [12]

Further, mathematical models of the two systems were formulated for comparison to the experimental data. The right image of Figure 5 displays the expected peak-to-peak voltage as a function of driving frequency for both the nonlinear (solid line) and linear (dashed line) cases. The surprising similarity between the theoretical predictions and the experimental data goes to show that mathematical descriptions of

nonlinear harvesters—though much more complicated than linear systems—are certainly possible and able to provide accurate predictions in the correct circumstances.

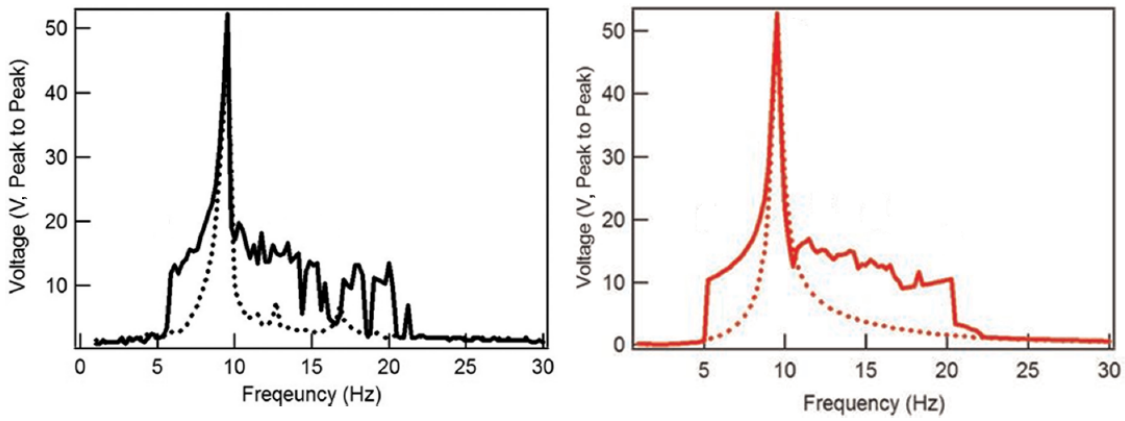

FIGURE 5: Piezoelectric response voltage of the cantilever beam system described in [12] for the nonlinear case (with the opposing magnet, solid line) as opposed to the linear case (without the opposing magnet, dashed line). The experimental data is shown in the left image as compared to the theoretical prediction, shown in the right image. [12]

As one can clearly see, the nonlinear system produces a significant response amplitude over a much wider (roughly 5 to 7 times) bandwidth than the linear cantilever case. Although this is a promising result, it should be noted that this specific device does not lie within the MEMS regime; the cantilever and proof mass have a combined mass of 3.2 g, while the cantilever itself is 4.4 cm in length. These dimensions are quite a bit larger than desirable for small power applications; further, this specific nonlinear design may be limited to larger scales due to the difficulty of combining permanent magnets to MEMS-scales geometries and perhaps also by the poor scaling quality of the magnetic field.

Buckled structures potentially offer the desired nonlinear response and bandwidth as described above while avoiding more complicated design and fabrication issues that magnetic systems bring about. One such simple buckled system [13] is illustrated in Figure 6; this design consists of a main buckled structure with a centralized proof mass and two offset piezoelectric harvesting components. Although this implementation is slightly larger even than the magnetic nonlinear system described above,

the premise of a buckled structure allows for much greater ease in scaling down to a MEMS scale. For instance, one can imagine the simplest of buckled designs as a compressively stressed, doubly-clamped simple piezoelectric beam, which lies well within the feasibility of MEMS microfabrication.

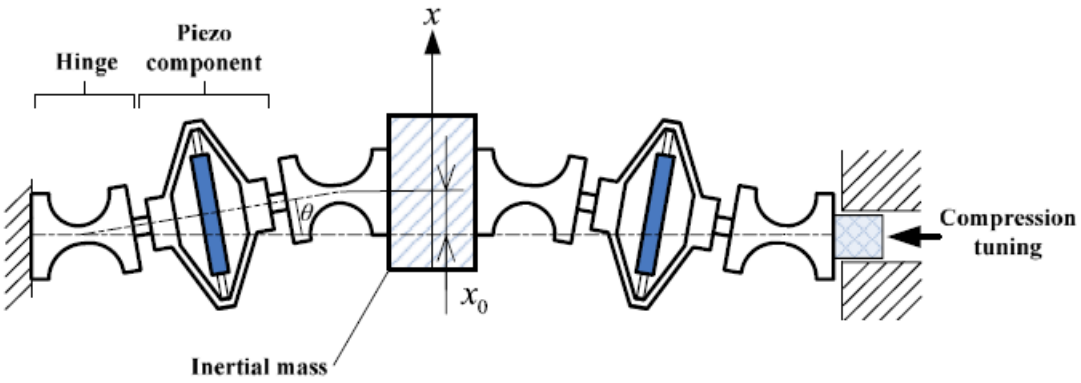

FIGURE 6: A simple buckled harvester design with a central proof mass and two offset piezoelectric energy gathering components. [13]

Similar to the results given for the magnetic nonlinear system, output power results for the buckled nonlinear harvester are illustrated in Figure 7; this specific data corresponds to an initial "chirp" excitation of 3 m/s^2 to the device. As before, the experimental data of the generated power shows promising similarity to the theoretical predictions, giving significant power generation over a much larger range of frequencies than, say, that of the linear harvester generation illustrated in Figure 5. As shown, such a harvester design claims a potential operating range spanning 24 Hz of near- or above-mW output levels.

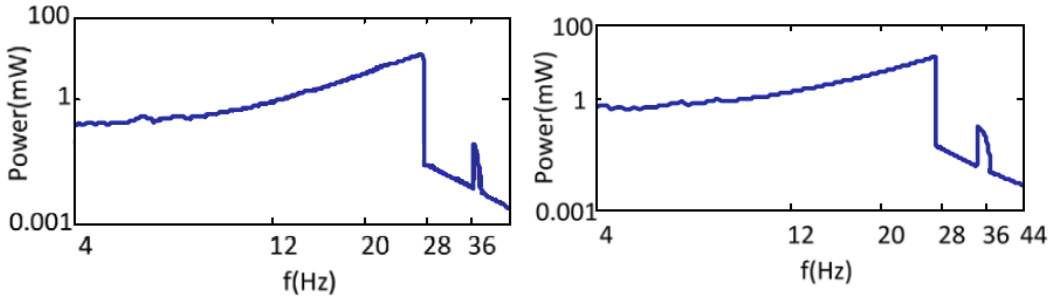

FIGURE 7: Power output as a function of frequency for the buckled nonlinear harvester discussed in [13]. The left plot displays experimental data while the right displays theoretical predictions. [13]

These nonlinear devices have proven to be successful in the centimeter scale size regimes. The remaining challenge is to carry these successful characteristics—namely a relatively small resonance frequency with a large operating bandwidth—into the millimeter scale via microfabrication techniques; thus is the goal of the research of this thesis. The remaining text is devoted to the design, fabrication, testing, and experimental results of a novel bistable buckled beam energy harvester in the hopes of developing a functional and effective MEMS PEH.

III. THEORETICAL DESIGN

A. Intended Structure and Operation

A macroscale model of the proposed device has been shown in Figure 2 of Chapter 1, displaying the buckled nature of the device. Unlike the simply buckled beam of Figure 6 which is supported only at the ends of the beam, this device is also anchored in the center of the beam length, creating three nodal points in total. In such a geometry, the beam shape is sensitive to torques applied to this central node, since the beam rotates about this point when snapping between its two states. In order to induce state-switching in vibrational environments, torsional level arms with proof masses are fixed to the pivot arms which anchor the central beam node. The lengths and masses of these lever arms can theoretically be tuned to the resonant frequency range of the ambient vibrations.

In addition, it is intended that the nonlinear characteristics of this harvester design will yield benefits similar to the expanded frequency range of Figure 5, in addition to an increased sensitivity to vibrations of lesser amplitudes. Further, it is reasonable to theorize that the snap-through behavior of a buckled beam allows for greater induced voltage—and thus harvestable current—than a cantilever design due to the large changes in strain which occur in very short periods of time during state-switching. In conclusion, the proposed device is a MEMS PEH which promises the potential for the wide-frequency-band harvesting, greater sensitivity, and increased output of other nonlinear harvesters while remaining a small-scale device with design parameters that can be easily tuned to the ambient vibrations of the device's application environment.

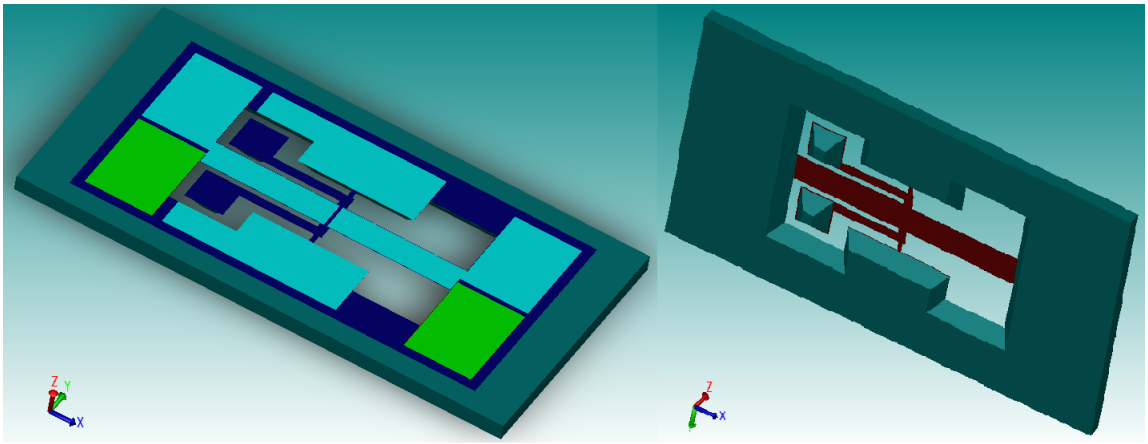

FIGURE 8: A computer model of the completed harvester design from a top-down view (left) and bottom-up view (right) generated using Coventorware MEMS simulation software.

Unlike the macroscale model, the intended operating scale of this proposed device lies in the mm range. A Coventorware MEMS model of the device is displayed in Figure 8. Microfabicration techniques—most importantly, photolithography—are needed in order to accurately develop a device at such a scale. Of course, photolithography necessitates the design of photomasks used to pattern each material layer of the device. The following sections are dedicated to the design layout of the device in terms of these photomask patterns.

B. Basic Device Layout

The fabrication of the proposed device requires five photomasks corresponding to patterning of the following material layers or processes: stressed silicon nitride, bottom electrode, piezoelectric, top electrode, and the final bulk etching step. These masks are displayed in Figure 9 superimposed on top of one another. In Figure 10, each process step is overlapped only with the preceding/upcoming photomask to gain an understanding of the development process as it occurs in real fabrication.

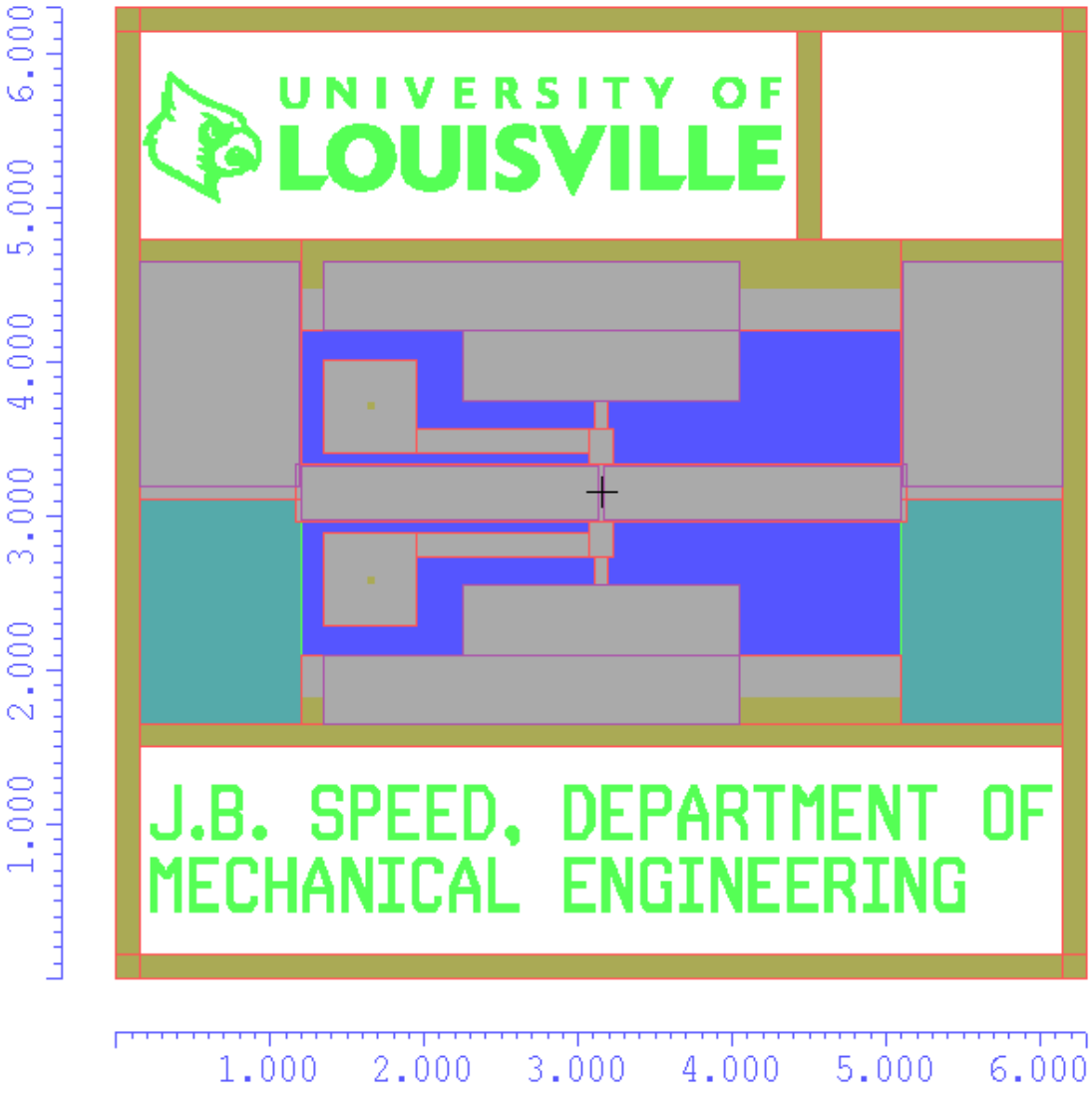

FIGURE 9: Superimposed layouts of all five device photomasks: bulk etching (blue), stressed nitride (green), bottom electrode (cyan), piezoelectric (red), top electrode (violet). (Scale in millimeters.)

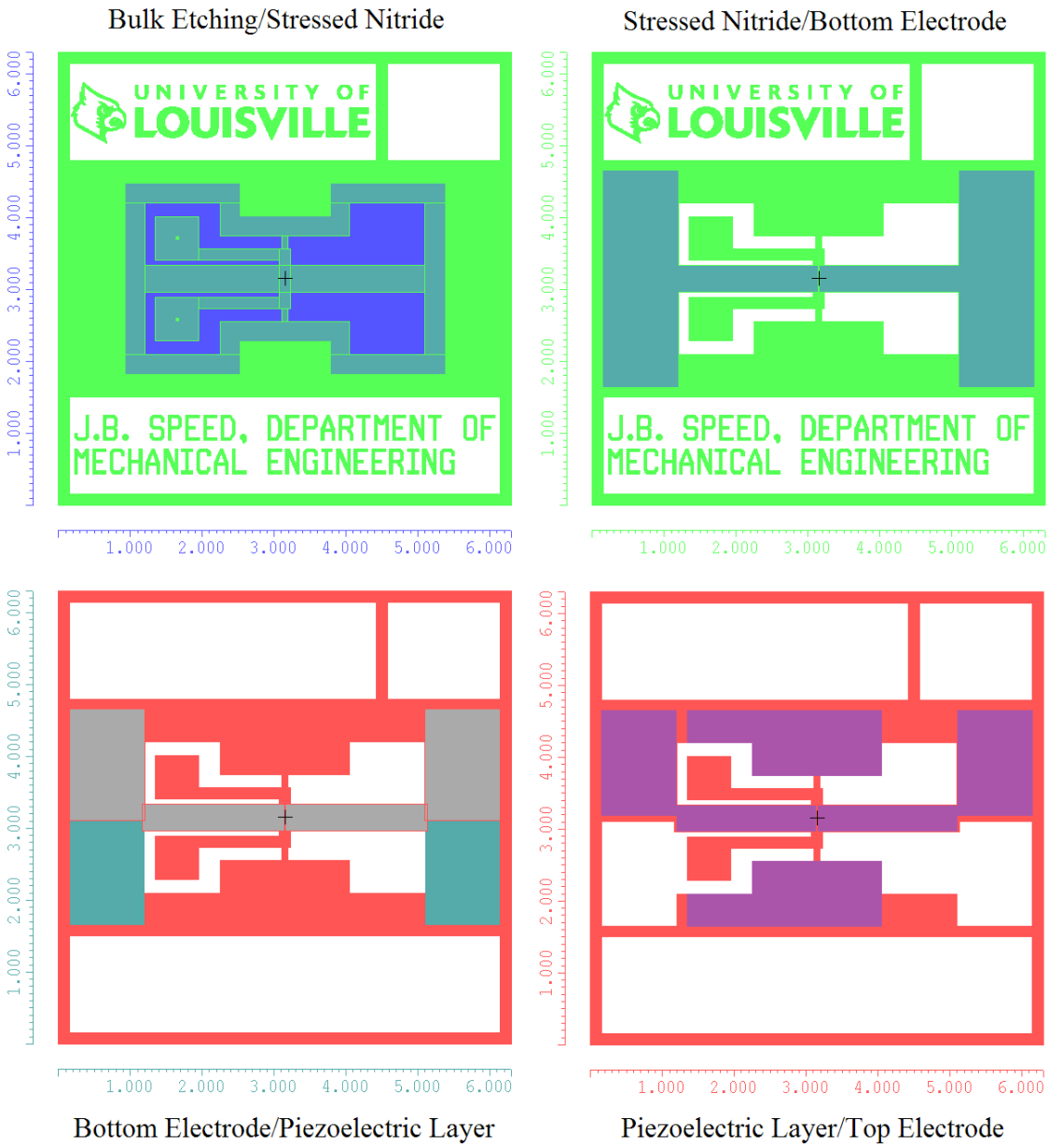

FIGURE 10: Device photomasks overlayed against preceding/upcoming mask layouts in terms of device fabrications: bulk etching (blue) and nitride (green), top left; nitride (green) and bottom electrode (cyan), top right; bottom electrode (cyan) and piezoelectric (red), bottom left; piezoelectric (red) and top electrode (violet), bottom right. (Scale in millimeters.)

Stressed Nitride

A stressed silicon nitride layer is the first layer to be patterned (Figure 11) after its PECVD deposition in a typical process flow. This material provides the structural foundation of the beam, including the compressive stress required to induce buckling. This layer provides the support not only for the main beam, but also for lever arms, the anchoring pivot arms, and the foundations for the electrode pads. In addition, this layer provides the text to be seen on each completed cell.

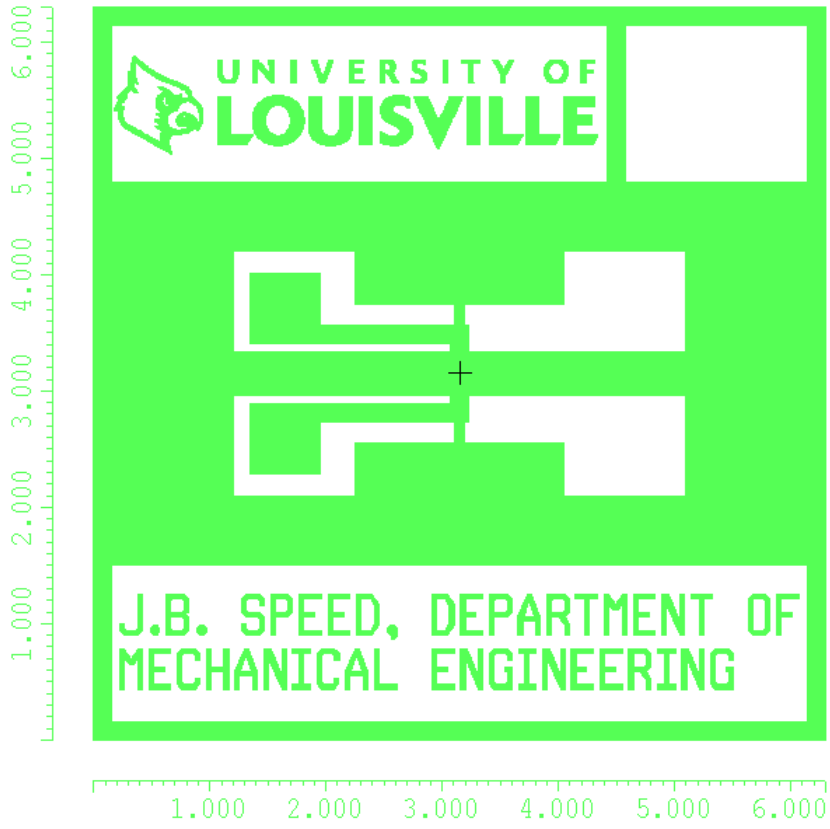

FIGURE 11: The photomask layout corresponding to the stressed silicon nitride layer, which provides the support and foundation for the entire device and which is responsible for the compressive stresses within the beam. (Scale in millimeters.)

Bottom Electrode

A bottom electrode is patterned next (Figure 12). This layer is to be electrically connected to the bottom face of the piezoelectric layer and will provide wire bonding pads for testing and packaging completed devices. It is important to note that each half of the beam electrode is separated since these halves will generate opposing currents due to the opposite signs in strains they experience. In the orientation shown, the bottom half of each large electrode pad at either end of the beam length will remain uncovered in order to provide an electrical contact surface. The remaining portions of the electrode will be covered by the piezoelectric layer and the top electrode.

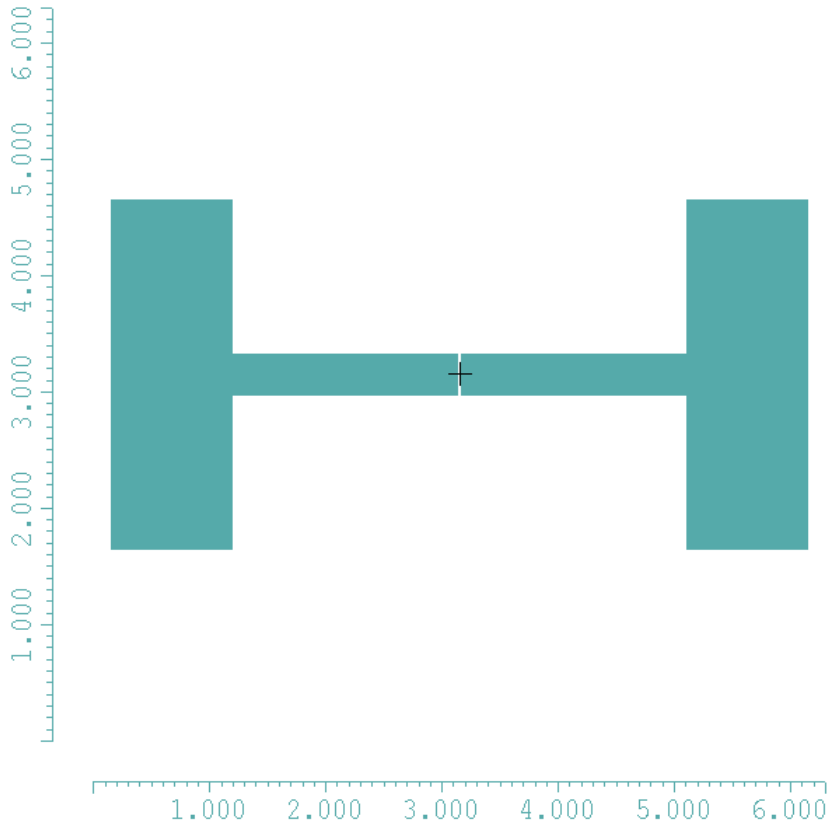

FIGURE 12: The photomask layout corresponding to the bottom electrode layer, which provides electrical connectivity to the underside of the piezoelectric layer. (Scale in millimeters.)

Piezoelectric Layer

The important piezoelectric material is deposited and patterned (Figure 13) between the electrode layers. This layer is responsible for the generation of harvestable current produced between the two electrodes during vibration loading. The material also provides an even foundation for the top electrode to be deposited afterward.

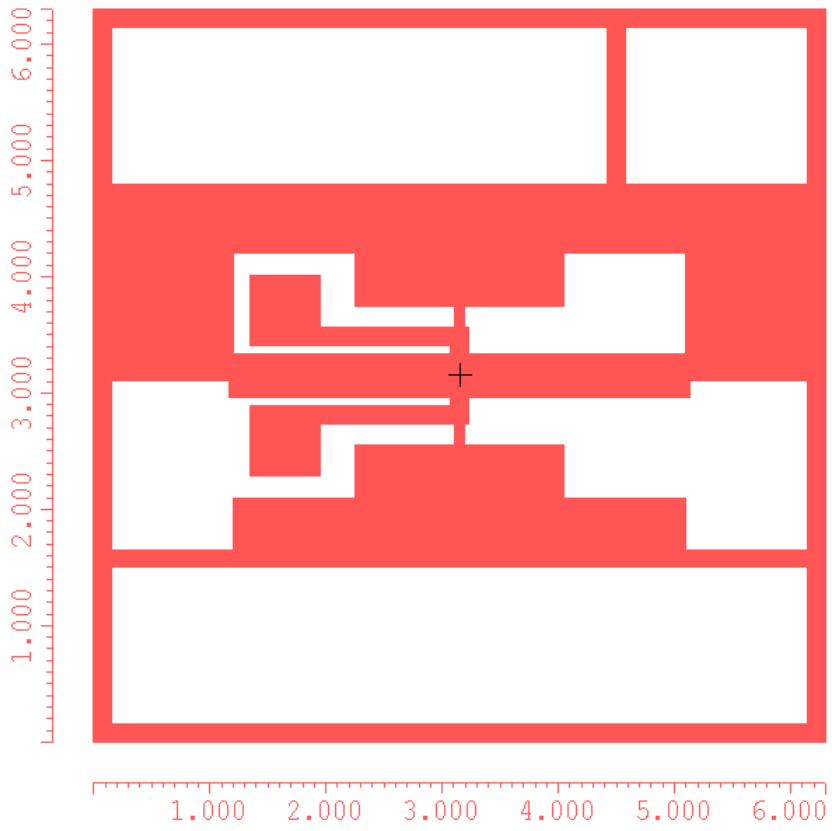

FIGURE 13: The photomask layout corresponding to the piezoelectric layer, which is responsible for the current generation between the electrodes upon the beam's state-switching. (Scale in millimeters.)

Top Electrode

The top electrode is the final structural layer to be patterned (Figure 14). This layer provides electrical connectivity to the topside of the piezoelectric layer. Similarly to the bottom electrode, this layer provides wire bonding pads for testing and packaging. However, in addition to the normal beam electrode pads, this layer also provides two separate pads on either side of the beam for the purposes of real-time capacitance measurements (as a method for deducing the beam's buckling frequency during dynamic testing).

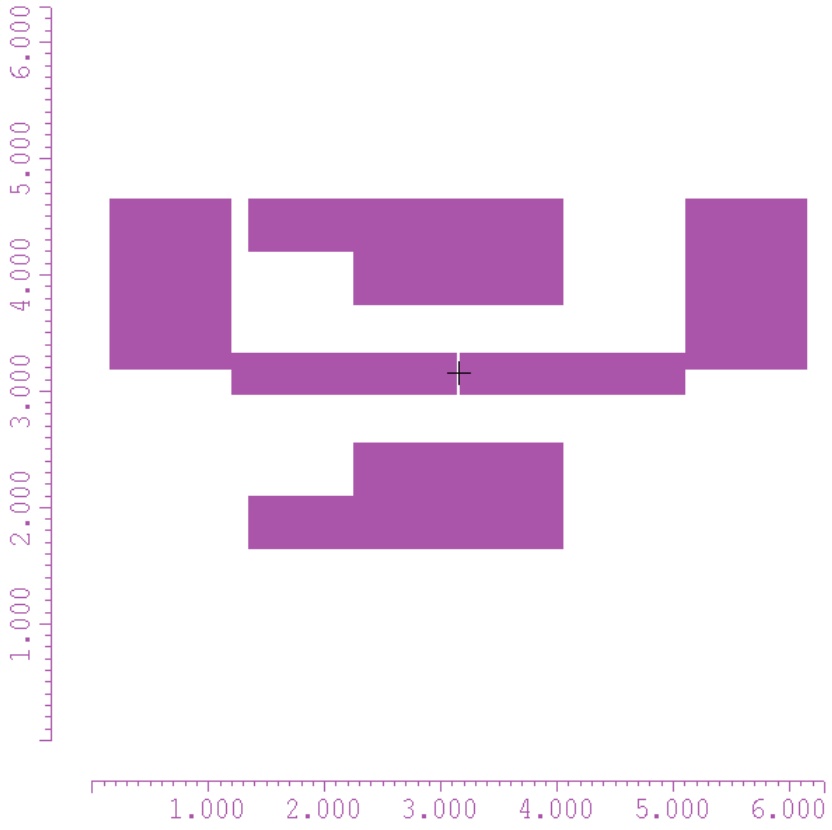

FIGURE 14: The photomask layout corresponding to the top electrode, which provides electrical connectivity to the top surface of the piezoelectric layer. (Scale in millimeters.)

Bulk Etching

The final step of the device processing involves freeing the top side structures via bulk etching from the back side of the wafer. This etching is bounded by the mask window provided by the geometry displayed in Figure 15. The etching technique used in this research is KOH wet etching, which etches straight walls into the substrate at a precise $\arctan\sqrt{2} = 54.7°$ angle. Due to this effect, the backside etching windows need to be padded along all dimensions by an additional width of $h/\sqrt{2}$ for a wafer height h in order to create the desired geometry at the top side; for the 380 μm thick wafers used in this research, the additional window padding required is about 268 μm.

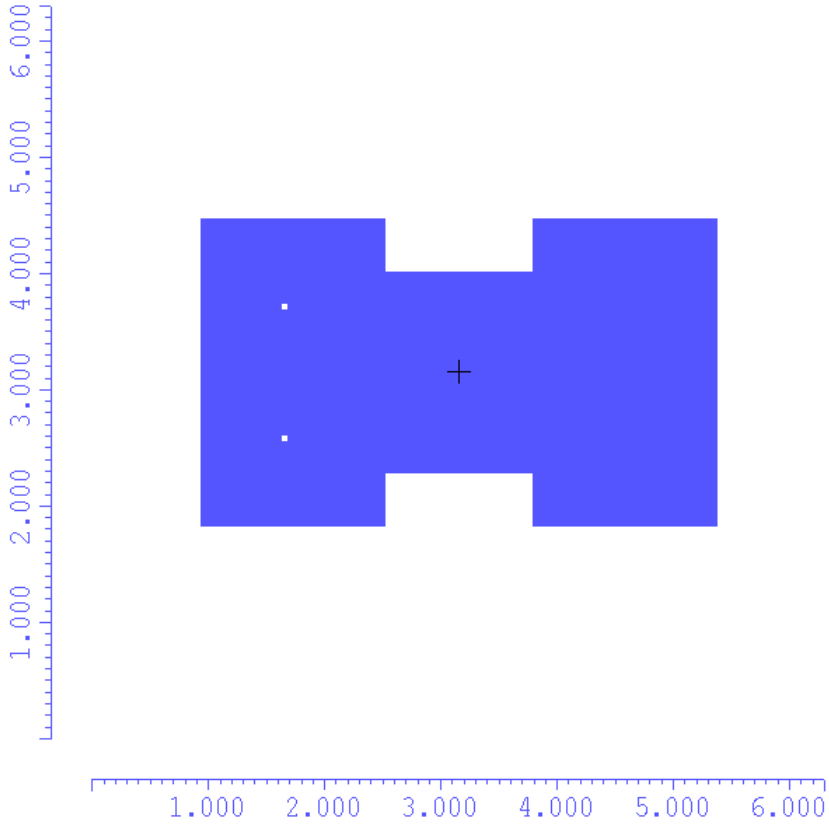

FIGURE 15: The photomask layout of the back side etching window required to produce the correct topside geometry via a KOH bulk etching process. (Scale in millimeters.)

This increase in size along all edges is observed in the top-left overlay of Figure 10, where the blue etching window appears oversized when compared against the free space of the green nitride geometry.

C. Auxiliary Device Designs

While the device design described in the previous section is the simplest (and perhaps easiest to successfully create) bistable buckled beam harvester design of this type, several additional "auxiliary" designs were created for larger or more complicated harvesters which utilize the same working principal. Compared to the basic single-node design, two of these harvesters implement multiple nodes across a longer beam length. Another alternative harvester is very similar to the basic single-node design except that all its dimensions are scaled up in order to create a longer, wider single-node beam. Additionally, two types of testing cells were designs for the purposes of film stress analysis and piezoelectric harvesting properties: one type is a standard cantilever beam weighted with a square proof mass, while the other is a simple beam fixed at both ends.

The designs which implement a beam shape with multiple nodes allow for a significantly longer beam, which promises greater harvesting capabilities (assuming the beam is still readily able to switch between its two stable states). Additionally, if the number of nodes along the beam length is an even number, then the device can be designed with the lever arms and proof masses attached at both ends for double the effectiveness of the state-switching actuation. Of course, having several nodes across the length of a beam may prove difficult in practice to successfully fabricate. Even so, multiple node designs hold promise of several theoretical benefits in spite of any fabrication difficulties. Two versions of multiple-node harvesters were designed. The photomask layouts of a two-node device are displayed in Figure 16, while the layouts of a four-node device are shown in Figure 17.

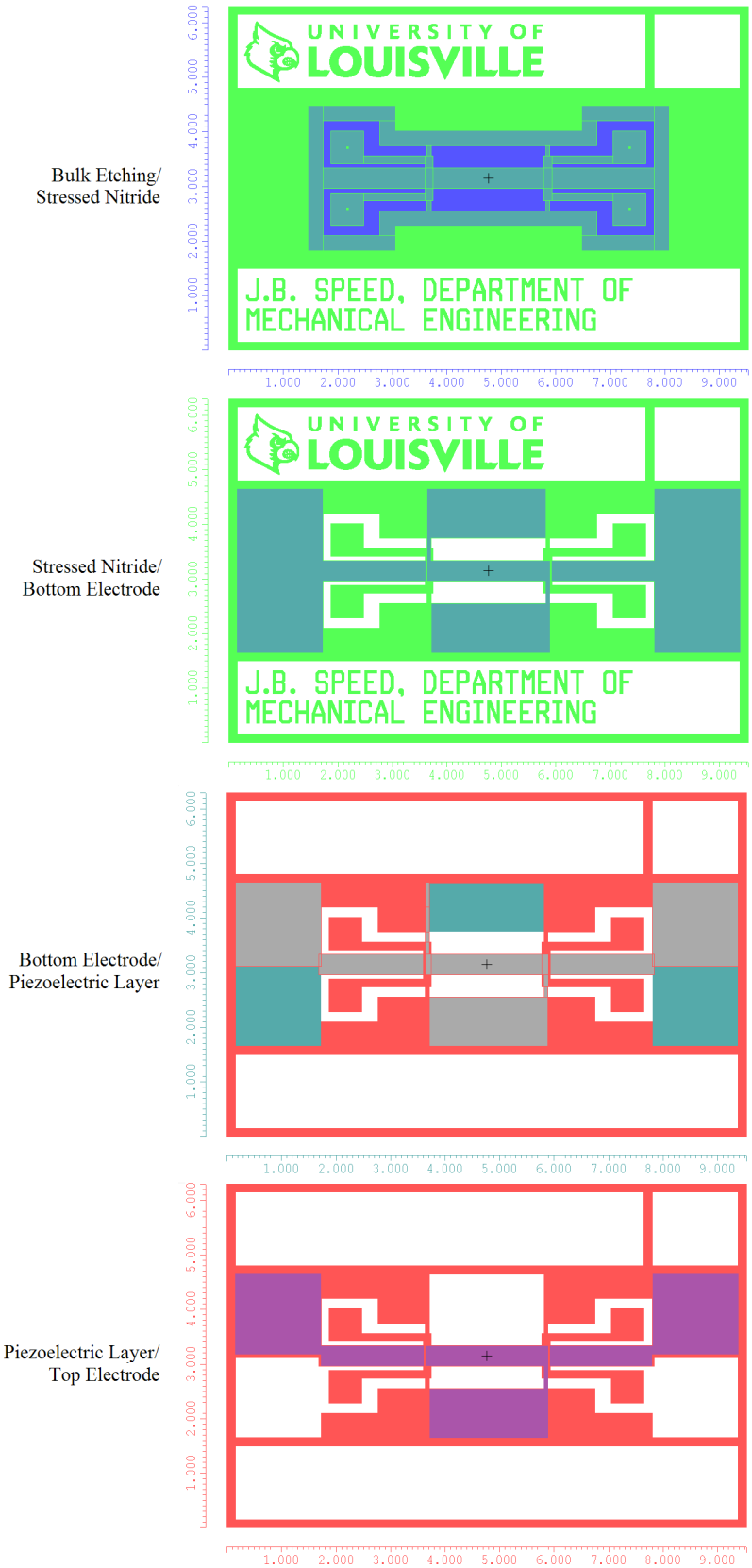

FIGURE 16: All five photomasks of the two-node, medium length harvester design layout, overlayed in terms of fabrication order. (Scale in millimeters.)

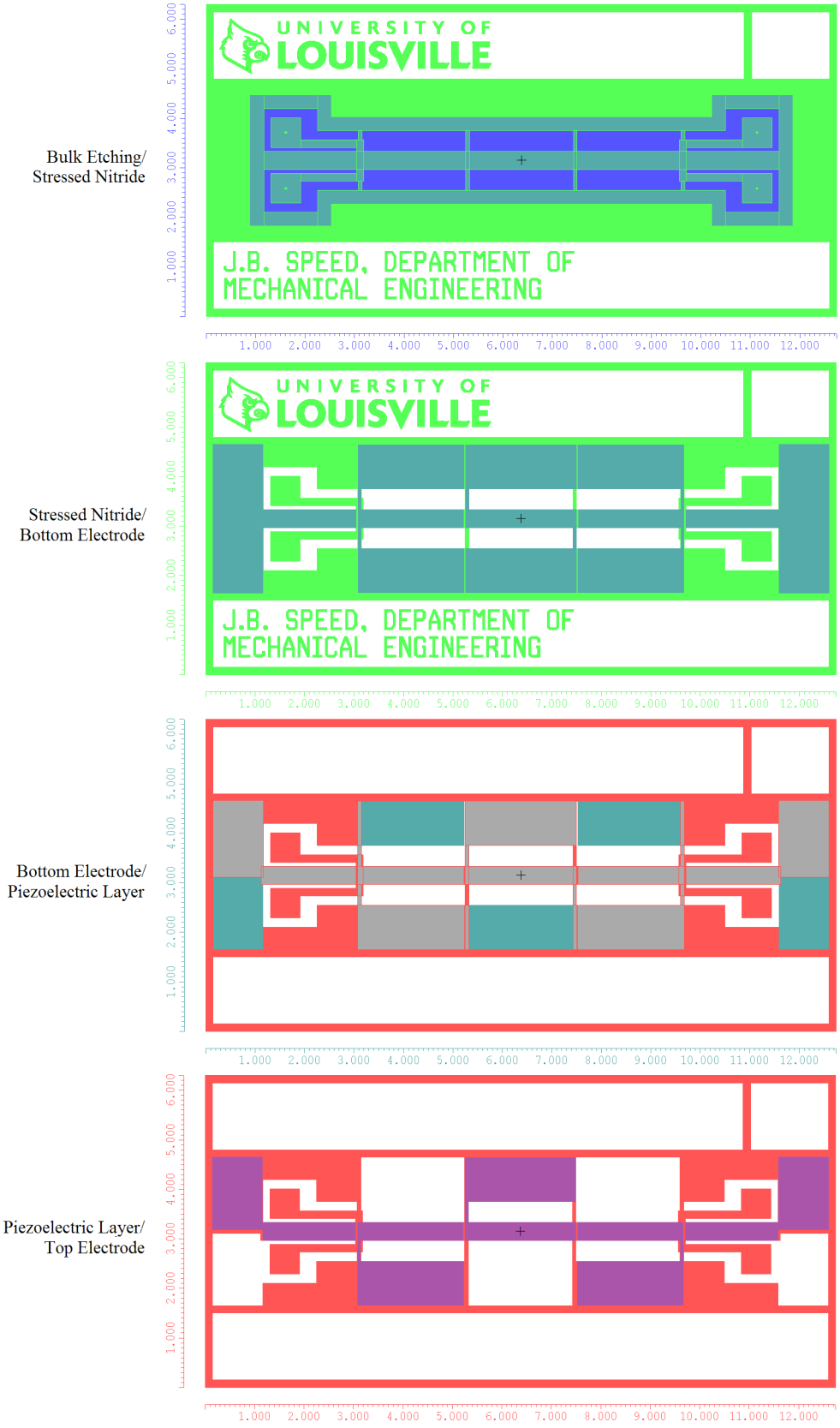

FIGURE 17: All five photomasks of the four-node, long length harvester design layout, overlayed in terms of fabrication order. (Scale in millimeters.)

The dimensions of the large single-node device have been increased from the original design by roughly 150%. The increased surface area of the beam would allow for increased harvesting capabilities, as in the multi-node cases, while also tending to operate at lower frequencies due to increased mass. It is unknown beforehand whether this increased size would allow for easier or more difficult fabrication. The photomask layouts of the large single-cell design are displayed in Figure 18.

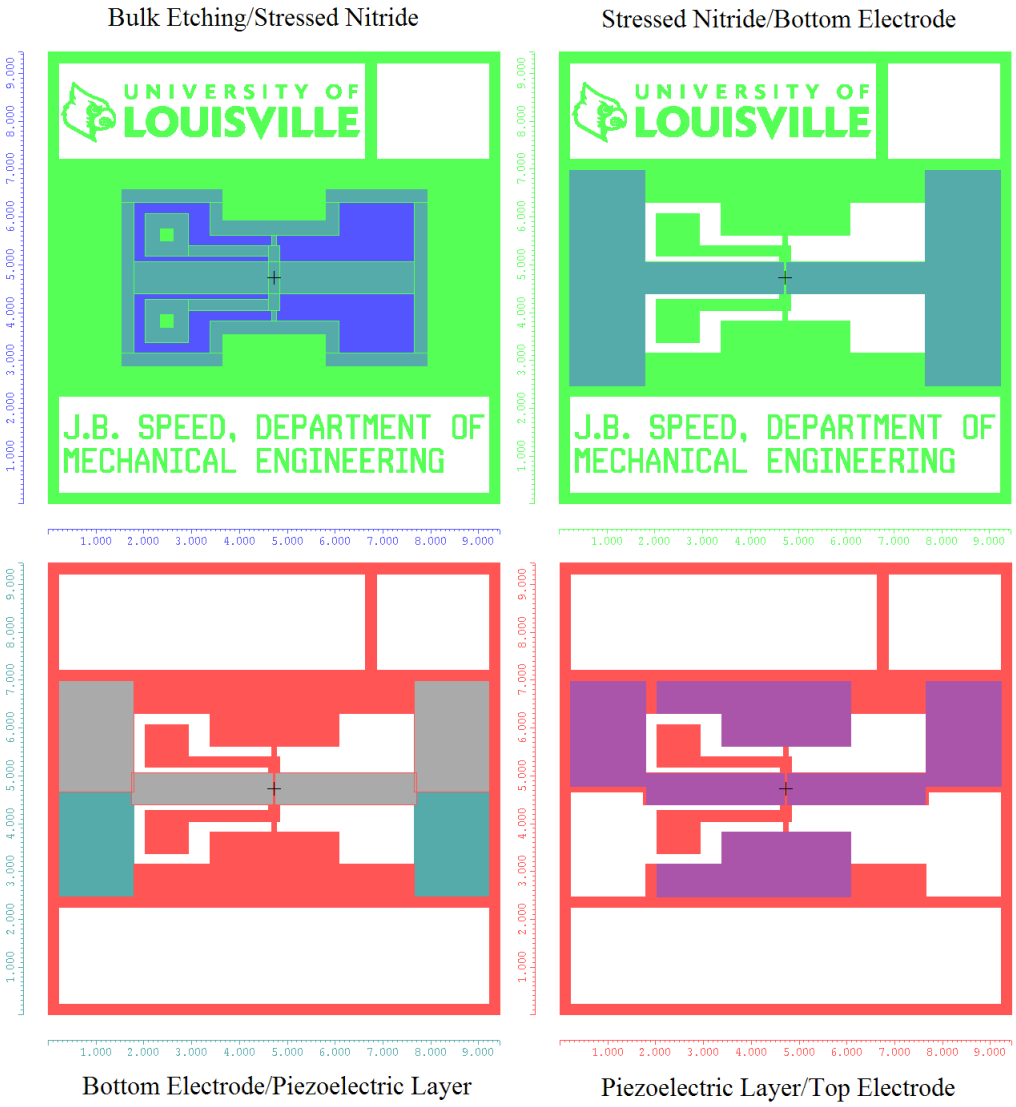

FIGURE 18: All five photomasks of the scaled-up large harvester design layout, overlayed in terms of fabrication order. (Scale in millimeters.)

The cantilever beam cell was designed as a control device for the purpose of comparing the harvesting capabilities of the new buckled, nonlinear designs with traditional, linear designs that have already proven to be somewhat successful. The photomask layouts of the cantilever design are given in Figure 19.

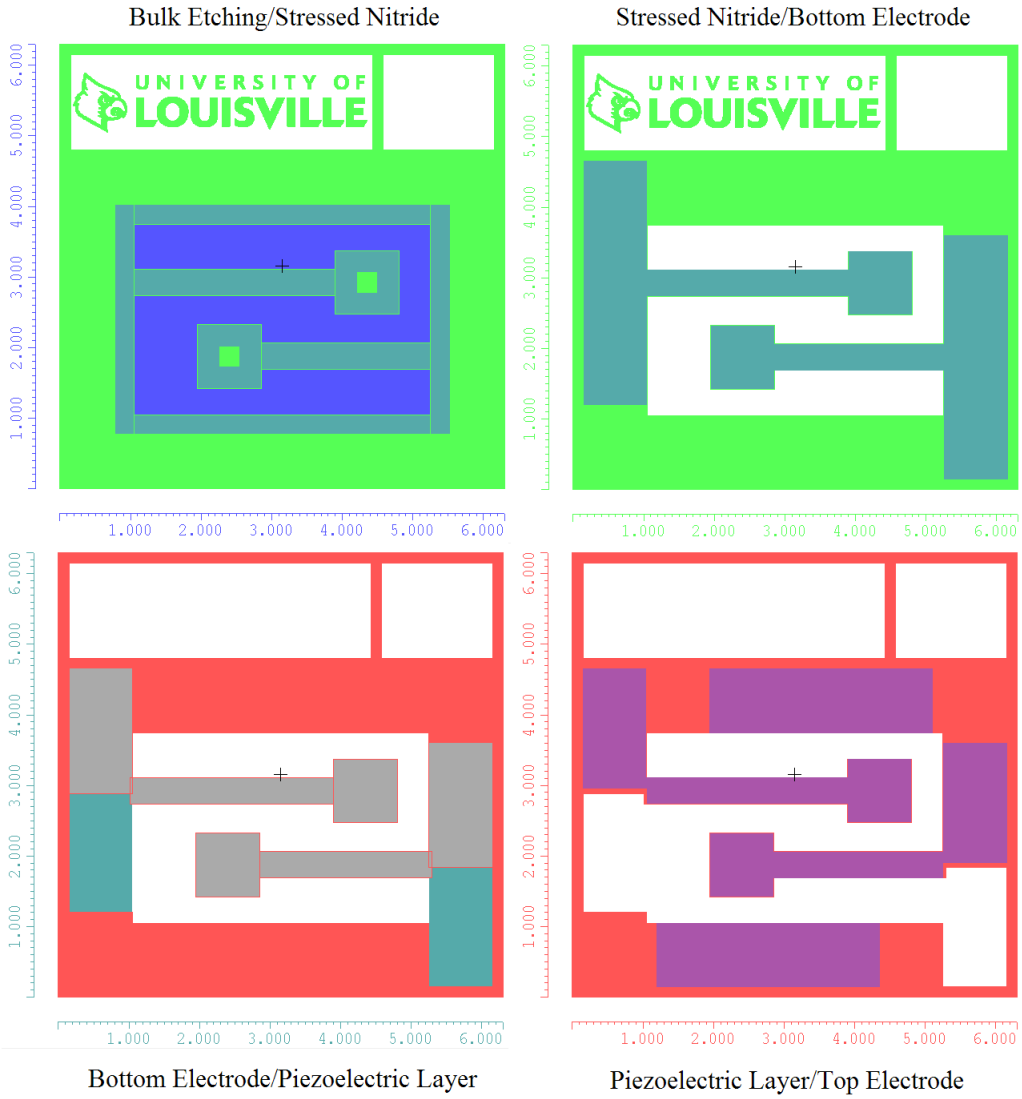

FIGURE 19: All five photomasks of the traditional cantilever beam harvester design layout, overlayed in terms of fabrication order. (Scale in millimeters.)

The simple ends-fixed beam cell was designed for the purpose of measuring the inherent stress within the deposited material layers (most notably the silicon nitride). It may also be useful in studying the buckling behavior of these cells as compared to that of the proposed buckled harvester designs. The photomask layouts of the simple beam are displayed in Figure 20.

FIGURE 20: All five photomasks of the ends-fixed beam design layout, overlayed in terms of fabrication order. (Scale in millimeters.)

D. Bulk Etching Simulation

In order to gain a better understanding of the anisotropic bulk wet etching step and the resulting cell geometry, an etching simulation software named ACES (Anisotropic Crystalline Etching Simulator) was used to generate simulated cells at varying stages of the bulk etching process. The basic single-node bulk etching photomask profile (Figure 15) was loaded into the software, in addition to the profile dimensions, silicon wafer thickness (380 μm), wafer crystalline plane orientation (100), and the wet etchant solution (45% KOH).

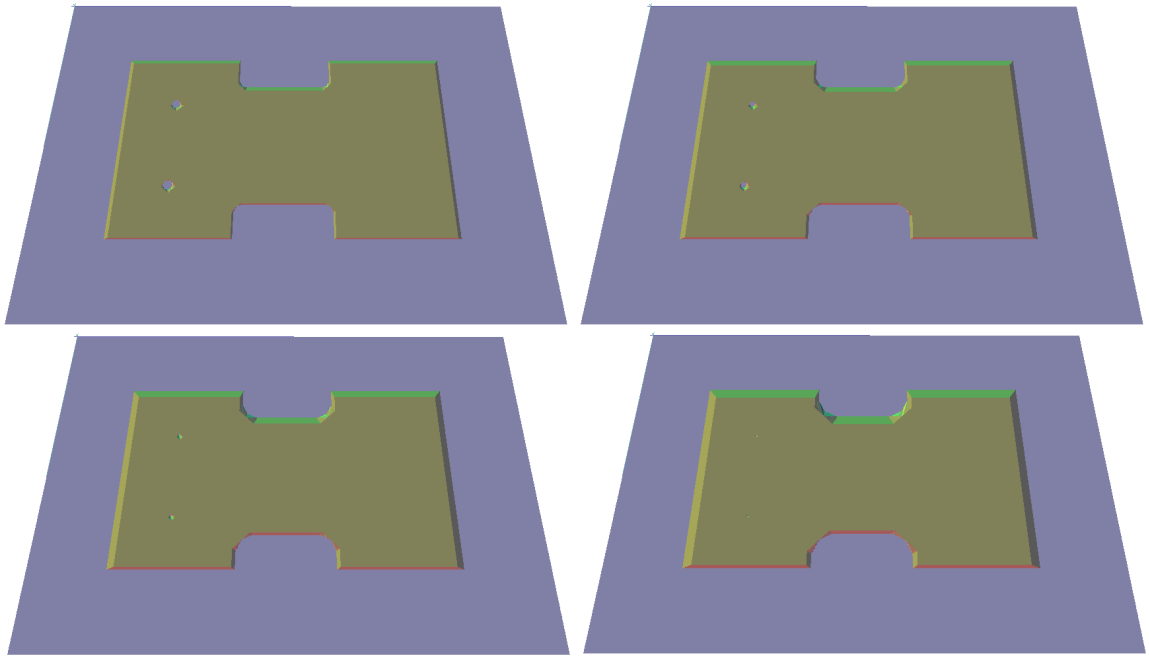

FIGURE 21: The simulated results (generated via the ACES software) of etching a single-node cell bulk etching photomask profile (Figure 15) after the elapsed times: 2 hours (top left), 3 hours (top right), 4 hours (bottom left), 5 hours (bottom right). Note that the convex corners of the mask profile become unexpectedly eroded; the lever arm proof mass mask profiles become completely eroded away during the etch.

Successive images of a five hour simulated KOH etch are displayed in Figure 21. One noteworthy observation provided by this simulation is the unexpected over-etching of convex corners in the substrate. Such an effect causes the substrate support structure on either side of the beam to erode much more than expected; similarly, the proof masses on the lever arms are etched almost entirely away after five hours (which is approximately the amount of time for KOH to etch vertically through the wafer.)

These results are less than ideal for the proposed harvester application: convex corner etching will primarily weaken the surrounding substrate support, possibly to the point that it compromises the integrity of the harvester material films. This effect will also render the technique of creating lever arm proof masses (by utilizing the properties of the anisotropic wet etch to leave pyramid-shaped masses attached to the lever arms while etching away the surrounding material) virtually impossible, unless the harvester design is increased significantly in size so that the convex corner etching has much less of an influence.

Of course, these results are still simply simulations. While the simulated etching process gives an idea of potential upcoming complications with the proposed design and process flow, the true experimental results of actual fabrication have yet to be discussed; beginning with experimental fabrication, these important facets of this research will be discussed in the remaining chapters.

IV. EXPERIMENTAL FABRICATION

A. Micro-Nano Technology Center

All microfabrication processes discussed in this research have taken place at the University of Louisville's Micro/Nano Technology Center (MNTC) [14]. This facility is a $10,000$ sq. ft., class 100/1000 cleanroom supporting micro/nanotechnology research across several areas of research, including mechanical engineering, chemical engineering, electrical and computer engineering, chemistry, physics, and medicine.

The cleanroom space is divided into designated bay areas supporting various fabrication processes, including thermal oxidation, material deposition, wet etching, dry etching, and photolithography. Other specialized tools (such as the scanning electron microscope used to generate material images found later within this chapter) needed for this research were accessed within the Huson Nanotechnology Core Facility (HNCF), which currently operates under MNTC.

In addition, the MNTC facility maintains tools designed for in-house photomask production, as well as access to software such as L-Edit and Coventorware for the purposes of layout design and modeling, as discussed earlier in this text. Further, the facility contains dicing, wire-bonding, and packaging tools for the final microfabrication steps in a typical process flow, once the device wafer in question has been fully and successfully fabricated.

B. Substrate and Oxide Layers

All experimental microfabrication explored in the research of this text begins with 4 inch pure silicon (Si) wafers. These wafers maintain a thickness of 380 μm and a (100) crystalline plane orientation. One surface (denoted the top or front surface) of the wafer is very finely polished for optimal surface fabrication; the opposite face (bottom side) remains unpolished and much rougher, and thus is less optimal for precise fabrication processes.

Neglecting the small amount of natural oxidation which has accumulated on the surface of these wafers, several wafers used in this research acquired a significant oxide layer through a thermal oxidation step before further fabrication. The details of this oxidation recipe are not fully characterized in this text since the thermal oxidation process is handled exclusively by MNTC personnel. The end result of the process is the addition of roughly 400 to 500 nm of thermal oxide to both sides of the involved wafers.

However, not all wafers of this research began with a thermal oxidation step; in fact, such a step is rather unnecessary for this research due to the following deposition of silicon nitride. Many microfabrication process flows begin with a deposition of silicon dioxide as a barrier layer or pattern mask, but the deposition of silicon nitride in the context of this research is preferable due to its great resistance to a KOH etching solution.

C. Silicon Nitride Deposition

Silicon nitride is crucial to the proposed device for two distinct reasons: one, a stressed nitride layer is responsible for beam buckling; and two, an unstressed nitride layer is used as a patterned protection of the back side of the wafer during KOH etching.

The main difference between the depositions of the two nitride layers is the inherent stress, which is controlled via pulsing or not pulsing the high- and low-frequency power used in the plasma-enhanced chemical vapor deposition (PECVD). Both recipes use the MNTC's Oxford PECVD system for nitride deposition.

Stressed Nitride

The stressed silicon nitride recipe takes place over a 25 minute deposition time at a chamber pressure of 650 mTorr. The heater temperature is set to 350° C while the chiller is set to 70° C. The gas flows are as follows: 400 sccm of 5% SiH_4/Ar, 600 sccm of N_2, and 20 sccm of NH_3. Both the high- and low-frequency power are set to 50 W at 10 second pulse lengths.

The resulting inherent stress within the layer (as measured by a Toho stress measurement system) varies quite significantly, ranging between -200 MPa and -600 MPa. The layer thickness (as measured via a Dektak profilometer) seems fairly consistent at an average value of about 560 nm.

Unstressed Nitride

The unstressed, protective nitride is deposited in much the same way as the stressed layer. In this research, the deposition time, temperature settings, and gas flows are exactly the same as described above. However, the low-frequency power remains unused in this deposition, while the high-frequency power requires 50 W at a pulse length of 20 seconds. The chamber pressure is increased slightly to 850 mTorr.

The stress within the resulting layer is minimal, normally within 50 MPa in magnitude. Similarly to the stressed layer, 25 minutes of deposition time provides a thickness of roughly 560 nm. This amount of silicon nitride is more than enough to protect underlying silicon substrate from a KOH etching solution, since the etch rate of nitride in KOH is virtually negligible.

D. Metal Electrodes Deposition

All metals are deposited via physical vapor deposition (PVD) using a Kurt J. Lesker PVD 75 machine. For the majority of the research, molybdenum (Mo) was chosen as the bottom and top electrode material; however, aluminum (Al) is another common choice for an electrode material. Either deposition is performed using a 4 inch pure target material supplied with 500 W of power. The chamber, pumped for at least 45 minutes, is kept at a capman pressure of 6 mT. The deposition time is kept between 10 and 15 minutes.

For a molybdenum deposition, the resulting layer yields an inherent tensile stress on the order of 20 MPa. For a 10 minute deposition, the layer thickness is approximately 300 nm, while this value rises to roughly 450 nm for a 15 minute deposition (at a rate of about 30 nm per minute).

E. Piezoelectric Deposition

Common piezoelectric materials used within the energy harvesting community include lead zirconate titanate (PZT), polyvinylidene difluoride (PVDF), and aluminum nitride (AlN). While all three are applicable to the proposed device of this thesis, only the depositions of AlN and PVDF will be experimented within the fabrication research. PZT requires a high-temperature curing step which could potentially release much of the important compressive stresses built into the nitride layer needed for the beam buckling; for this reason, it is not an ideal harvesting material to be used in this specific harvester design.

The other two materials are tested in both the fabrication and experimentation stages, especially noting the ease and quality of the material deposition, and most importantly the mechanical and piezoelectric properties of the resulting material film in terms of vibrational energy harvesting. Both materials require significantly more

complex and difficult deposition recipes than the other materials used in this research. Nevertheless, the piezoelectric material is by far the most important for the functionality of the device and thus cannot be avoided.

AlN

Aluminum nitride is deposited via a heated PVD in combination with added gas chemistry, according to a recipe adapted from [6]. A 4 inch pure Al target is loaded into the chamber before pumping for at least one hour. In this time, the chamber temperature and auto setpoints are set to 300° C. Once the chamber is properly heated and sufficiently pumped, the gas chemistry is introduced. Argon and nitrogen gases are applied in an approximate 3-to-1 proportion, respectively; maximal setpoints of 7 sccm Ar and 20 sccm N_2 are recommend. This usage of the PVD machine requires the Source 3 gas and the Gas Injection buttons to be switched on.

Finally, the power can be introduced to the target in order to begin the deposition. However, it is noted that the addition of the nitrogen gases may cause the plasma to become somewhat unstable at higher powers. It has been found that increased plasma stability can be achieved by slowly increasing the applied load from relatively low power ($\approx 250-300$ W) to higher power ($\approx 450-500$ W) in small increments. Once the plasma is relatively stable, the wafer cover can be displaced and the deposition can begin.

This process of AlN deposition is quite slow. For a two hour deposition period, the resulting film thickness ranges between roughly 300 and 600 nm. In addition, this film retains an internal tensile stress on the order of 100 MPa. Finally, initial tests for piezoelectric properties display promising results, although additional work will be needed to further quantify these findings.

A sample of the deposited AlN material was examined via a scanning electron microscope (SEM). The observed material structure (Figure 22b) is compared to

similar images published in [6] (Figure 22a). It is seen that both samples exhibit a similar columnar, granular structure. These grains (and their size, density, and relative orientations within the material) affect the piezoelectric properties of the AlN film during straining. [6]

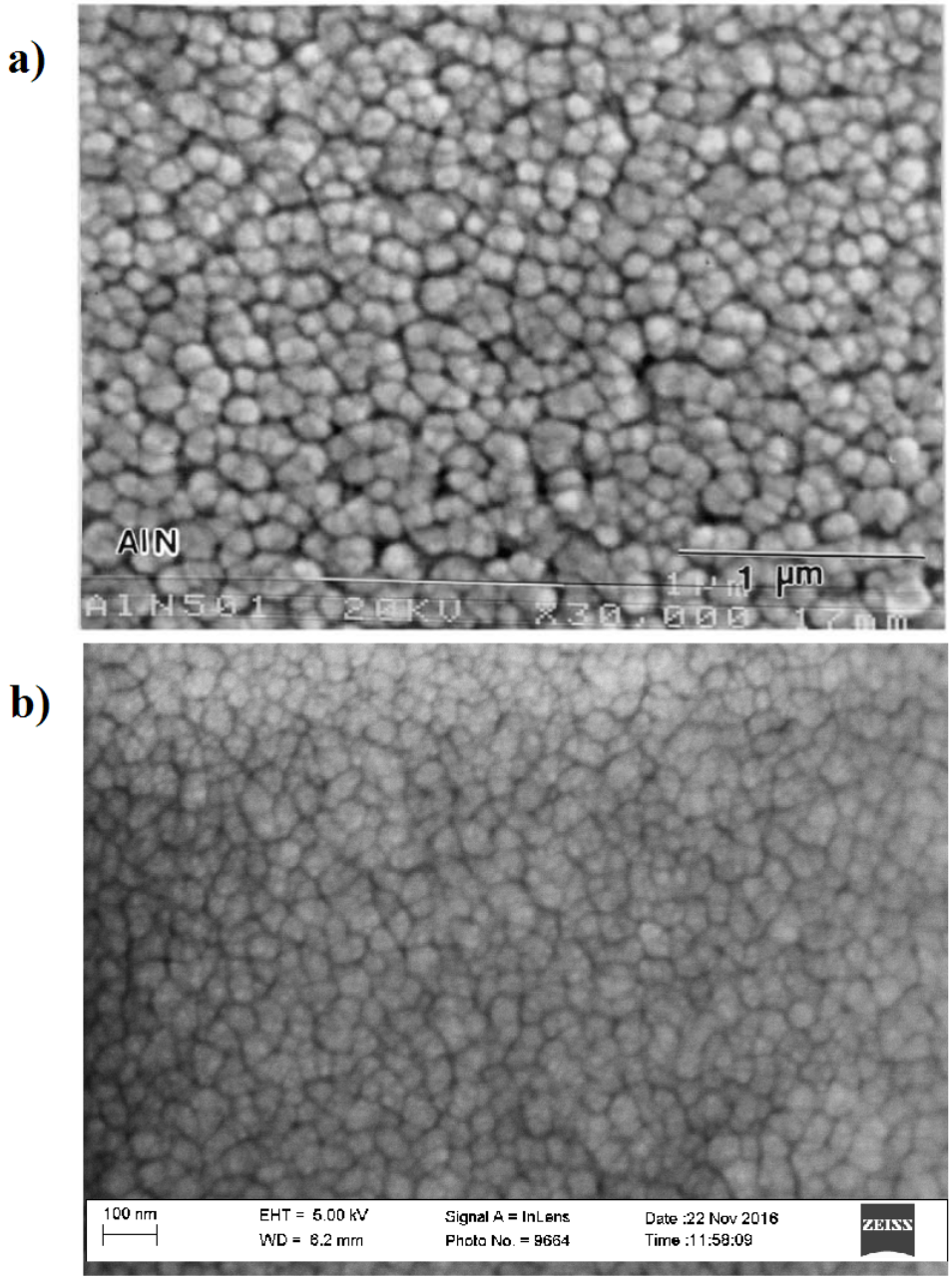

FIGURE 22: a) AlN material structure taken via SEM, as published in [6]. b) Similar image of experimental AlN deposition, as performed via the above recipe.

PVDF

Polyvinylidene difluoride is typically deposited via a sequence of spinning depositions and post-baking procedures, adapted from a recipe found in [15]. Firstly, a 75/25 molar ratio PVDF-TrFE powder (manufactured by Solvay) is dissolved into a Methyl Ethyl Ketone (MEK) solvent in order to produce two separate PVDF solutions: the first is a 5% PVDF solution (by weight), while the second is a 2% PVDF to MEK solution.

The first PVDF layer is deposited via spinning the 5% solution onto the wafer at 3500 rpm for 45 seconds. The wafer is then placed on a 105° C hotplate for 10 minutes in order to evaporate the solvent. This process is then repeated for the second layer deposition. After these first two depositions, the films are annealed in a 145° C oven for an hour. The third and final layer is deposited by spinning the 2% solution, evaporating the solvent, and annealing the combined films for at least three hours.

Unfortunately, a microscale profile of the resulting film displays a large amount of unevenness and porosity. The film thickness seems to range between roughly 200 nm and 2 μm. These characteristics make measurements of any piezoelectric properties extremely difficult (or impossible) since the film porosity allows electrical shorting to occur between the bottom and top electrodes. Additional work is needed in order to produce a more evenly distributed PVDF film across the wafer surface.

F. Photolithography

All photolithography processes discussed in this research followed the same recipe which has proven to be highly successful in producing crisp, clear protective masking layers. An example of such a layer is displayed in Figure 23, which depicts a patterned photoresist layer to be used as a protective mask during etching of excess molybdenum during the creation of the bottom electrode layer.

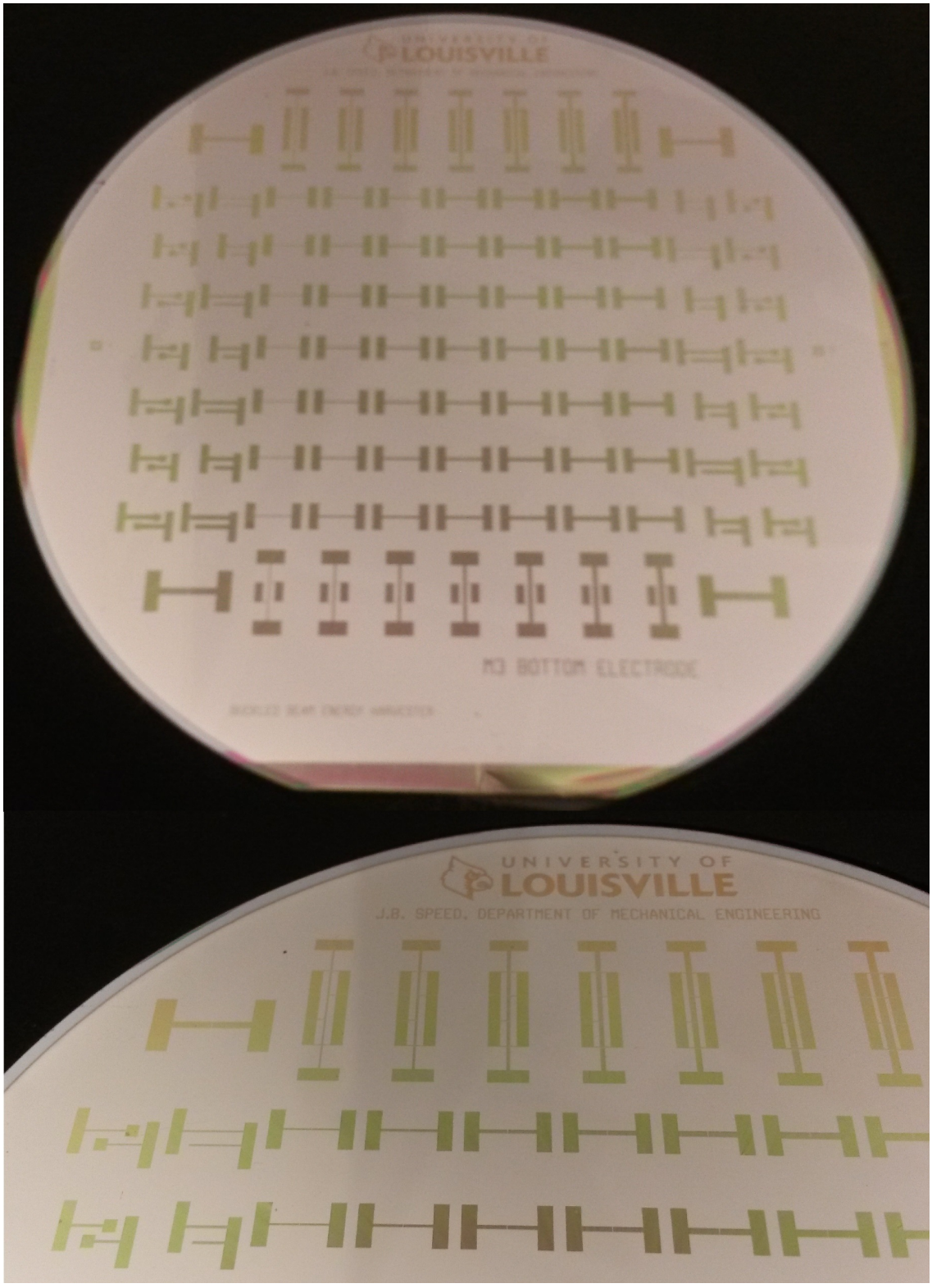

FIGURE 23: An example of a crisp photoresist masking layer. This specific layer is used as a protective layer during etching of molybdeum in order to produce a correctly patterned bottom electrode.

The process begins with the deposition of standard Shipley 1813 photoresist via spinning. The spinner recipe comprises a one second spreading step at 500 rpm (ramping at 500 rpm per second) followed by a ten second planing step of 4000 rpm (ramping at 500 rpm per second). The spinning is followed by a one minute rest on a 105°C to cure the photoresist.

The mask alignment and exposure steps are performed via a Suss Microtec Mask Aligner. Once the mask and wafer are properly aligned, an exposure of 12.1 mW/cm^2 intensity is applied for 12.0 seconds. The wafer is then placed on the hotplate for another one minute post-exposure heating step.

Finally, the wafer is placed into MF-319 developer for 50 seconds. The wafer is then promptly rinsed and dried completely. Finally, the wafer receives another one minute hotplate session for a post-development bake. At this point, this wafer is patterned with a hardened photoresist and is ready to undergo an etching process to eliminate unwanted material.

G. Surface Etching

All dry etching which takes place in this research is performed on a Trion Metal Etcher tool. The Trion utilizes a combination of reactive ion etching (RIE) and inductively cooled plasma (ICP) to etch material at a higher rate than a more traditional RIE system. Various gases are injected into the vacuum chamber at different flow rates in order to most effectively etch the undesired material in question.

Silicon Nitride

A silicon nitride etch utilizes a gas composition of 45 sccm CHF_3 and 5 sccm O_2. Typical etching requires a power of 75 W RIE and 300 W ICP at a pressure of 50 mTorr. The usual 560 nm nitride layer takes roughly 10 minutes to completely etch.

Molybdenum

A molybdenum etch uses the following three gases: 20 sccm Cl_2, 5 sccm O_2, and 5 sccm Ar. The process is performed at 50 W RIE and 300 W ICP power at a chamber pressure of 30 mTorr. A 450 nm Mo layer requires about 7 minutes of etching time.

Aluminum Nitride

An aluminum nitride etch requires a gas composition of 10 sccm BCl_3, 14 sccm Cl_2, and 6 sccm Ar. A power of 75 W RIE and 300 W ICP is applied at a 10 mTorr pressure. The typical range of AlN film thickness takes between roughly 2 and 5 minutes to completely etch.

Silicon Substrate

A pure silicon etch utilizes a gas composition of 30 sccm CHF_3, 10 sccm SF_6, and 2 sccm O_2. A large ICP power of 600 W is applied in conjunction with 75 W of RIE power at a chamber pressure of 35 mTorr. Since silicon substrate needs to be etched in large quantities (thicknesses significantly larger than 1 μm), the exact etching rate is not exactly quantified but it estimated to be on the order of 1 μm per minute.

Cured Photoresist

It is important that patterened photoresist be removed once it has provided the necessary etching mask for removal of the underlying excess material. Firstly, the cured photoresist can be quite thick compared to other structural device layers and may bring about undesired stresses or added rigidity. Secondly, any photoresist remaining between layers of the piezoelectric stack will not allow any electrical current flow to occur (since photoresist is a non-conductive, organic polymer) between the piezoelectric material and the electrodes and thus ruining the device.

In this research, excess photoresist is removed via a dry etch ashing technique (such a process works well for other polymers as well, including PVDF). A RIE power of 100 W and ICP power of 400 W are applied to 80 sccm O_2 at 50 mTorr. For a cured photoresist film resulting from the photolithography recipe described in the previous section, an etching time of 5 minutes works quite well.

H. Bulk Etching and Release

The most significant etching process required in the fabrication of the proposed device is the removal of the undesired substrate from beneath each device cell for the purpose of freeing the beam structure. In order to create well-defined window regions for each cell, isotropic methods (such as the ICP/RIE gas etching described above) cannot be applied since the substrate thickness is much greater than a normal thin film thickness.

Instead, an anisotropic etching technique must be employed to ensure a predictable and repeatable substrate window shape. It is noted that a deep reactive ion etch (DRIE) is the typical modern choice for such applications. However, per strict MNTC tool usage regulations, no metals are allowed to be placed within the DRIE tool available to this research; thus, any wafer that has been processed to the point of bottom or top electrode deposition is unable to be placed in the DRIE tool. Further, the DRIE step cannot at all be easily performed before the four main structural layers have been deposited and patterned: doing so would cause great problems regarding the strength of the topside layers during deposition and etching, the out-of-plane bowing of individual cell windows, and spinning photoresist due to lack of vacuum suction between the wafer and vacuum chuck. Due to these great difficulties, a less modern method must be employed to perform the bulk etching step.

A wet potassium hydroxide (KOH) etch is distinctly anisotropic, producing the well-known 54.7° angle in etching sidewalls due to significant differences in etching

rates of the various crystalline silicon planes. This important characteristic allows the exact window shape to be highly predictable and repeatable, in theory. However, there are several downsides to KOH etching: firstly, the KOH etching rate depends greatly on the temperature of the solution, and so any temperature discrepancies or gradients may cause significant variations in etching between any two wafers or cells within the same wafer; secondly, KOH etches at a very rapid rate (on the order of 1 μm/minute), allowing for quicker processing than other methods but at the expense of reduced control; thirdly, KOH is extremely destructive to most materials and thus provides little to no material selectivity (with the exception of silicon nitride, which etches at a negligible rate compared to any other material discussed in this research); finally, KOH is a very dangerous wet chemical and must be handled with extreme caution.

It is recommended to spin-coat the top side of the processed wafer with photoresist (cured for at least 3 minutes) to add protection against the remaining etching steps. If the wafer in question originally underwent a thermal oxidation step, then the oxide layers must be removed before the KOH etch. This removal is performed via a buffered oxide etch (BOE). For an oxide thickness of roughly 400 to 500 nm, the oxidized wafer requires roughly 7 to 10 minutes of BOE; the conclusion of the process is illustrated neatly by the clear hydrophobic behavior of the exposed pure silicon substrate within the back side windows.

Once the substrate of the back side windows are fully exposed, the wafer is ready for the KOH bath. A 45% KOH solution heated to 85° C is employed in this research. A one-sided wafer fixture is used to expose only the back side of the wafer to the KOH solution. To prevent bursting of the cells (which would then expose the processed front side of the wafer to the destructive KOH solution), it is recommended that no more than 350 μm of a 380 μm wafer be etched by the solution; if the window substrate thickness becomes any less than this, there becomes a great chance that

several windows will burst. It has been found that a total etching time between 4 hours, 20 minutes and 4 hours, 30 minutes is ideal for significant window etching without too great of a risk for window rupture. After half of the etching time has passed, the wafer is removed from the bath, rinsed, and is rotated 180° within the wafer fixture in order to provide a first-order cancellation of any depth-dependent etch-rate gradient within the KOH solution.

After the KOH bath is completed and has performed the majority of the necessary substrate etching, the wafer is diced into its individual cells. This step should be performed before completely releasing each cell beam structure so that the mechanical stresses induced during the dicing procedure do not rupture the extremely fragile thin films. The remaining 30 μm or so of substrate thickness should provide enough cell rigitidy to withstand dicing.

Finally, each individual cell is ready for the final release step. This process is carefully performed via a pure silicon etch within the Trion metal etcher. The cells undergo several ten minute etching trials until the beams have become completely freed. In addition, the protective top side photoresist layer must be entirely etched from each cell in order to provide electrical contact to the electrode bonding pads. At this point, the device has been completely fabricated and is ready to undergo testing.

I. Complete Process Flow

Various process flows have been explored throughout the length of experimental microfabrication research of this device, and the complete process given below has been established as the most effective flow in terms of ease, efficiency, and the quality of the resulting product. All deposition, etching, and patterning steps laid out in the following process flow refer precisely to the recipes given above and the design layouts explained in the previous chapter.

1. Deposit thermal oxide onto both sides of wafer*
2. Deposit unstressed silicon nitride onto back side
3. Deposit stressed silicon nitride onto front side
4. Pattern back side via bulk etching photomask
5. Etch excess back side unstressed nitride
6. Pattern front side via stressed nitride photomask (BSA**)
7. Etch excess front side stressed nitride and photoresist
8. Deposit molybdenum
9. Pattern via bottom electrode photomask
10. Etch excess molybdenum and photoresist
11. Deposit piezoelectric material
12. Pattern via piezoelectric layer photomask
13. Etch excess piezoelectric material and photoresist
14. Deposit molybdenum
15. Pattern via top electrode photomask
16. Etch excess molybdenum and photoresist
17. Spin protective photoresist onto front side
18. Etch back side oxide via BOE*
19. Etch back side substrate via KOH
20. Dice wafer into individual cells
21. Etch remaining substrate (and top side photoresist) to release structures

*These steps are not required in order to fabricate a functional device. In fact, it is recommended not to include these steps; they are given in this list only because thermal oxidation is a common practice and unprocessed wafers often begin with a thermal oxidation step.

**This is a *Back Side Alignment* (BSA) step. Such a process is often extremely difficult due to the lack of light and color variation within the back side alignment markers. In order to improve visibility, a razor blade is used to mark radial lines on the wafer outward from the alignment markers on the back side prior to the BSA.

This process flow is illustrated via Figures 24 to 30, displaying photos of an experimental wafer being processed according to the above steps.

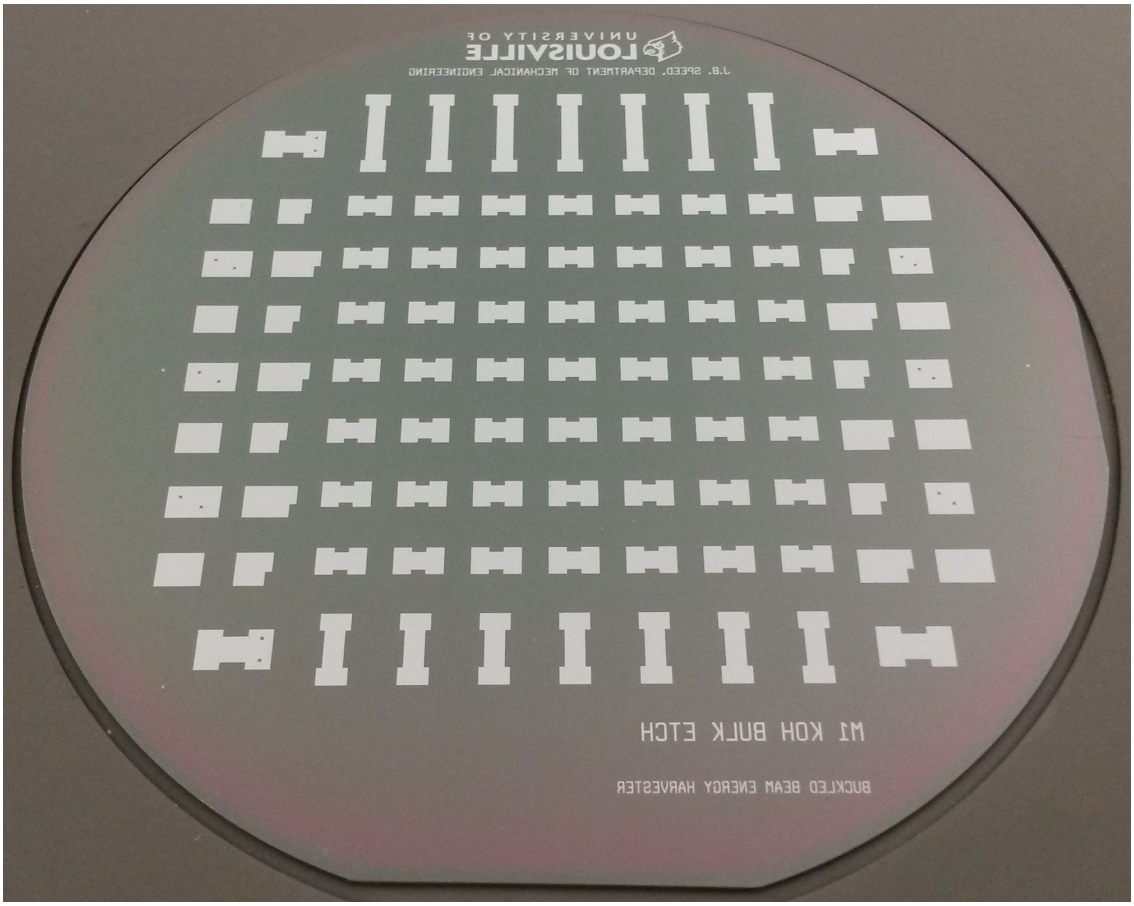

FIGURE 24: Processing photo following steps 1 to 5: depositing the nitride layers and patterning and etching the back side unstressed nitride layer with the bulk etching mask.

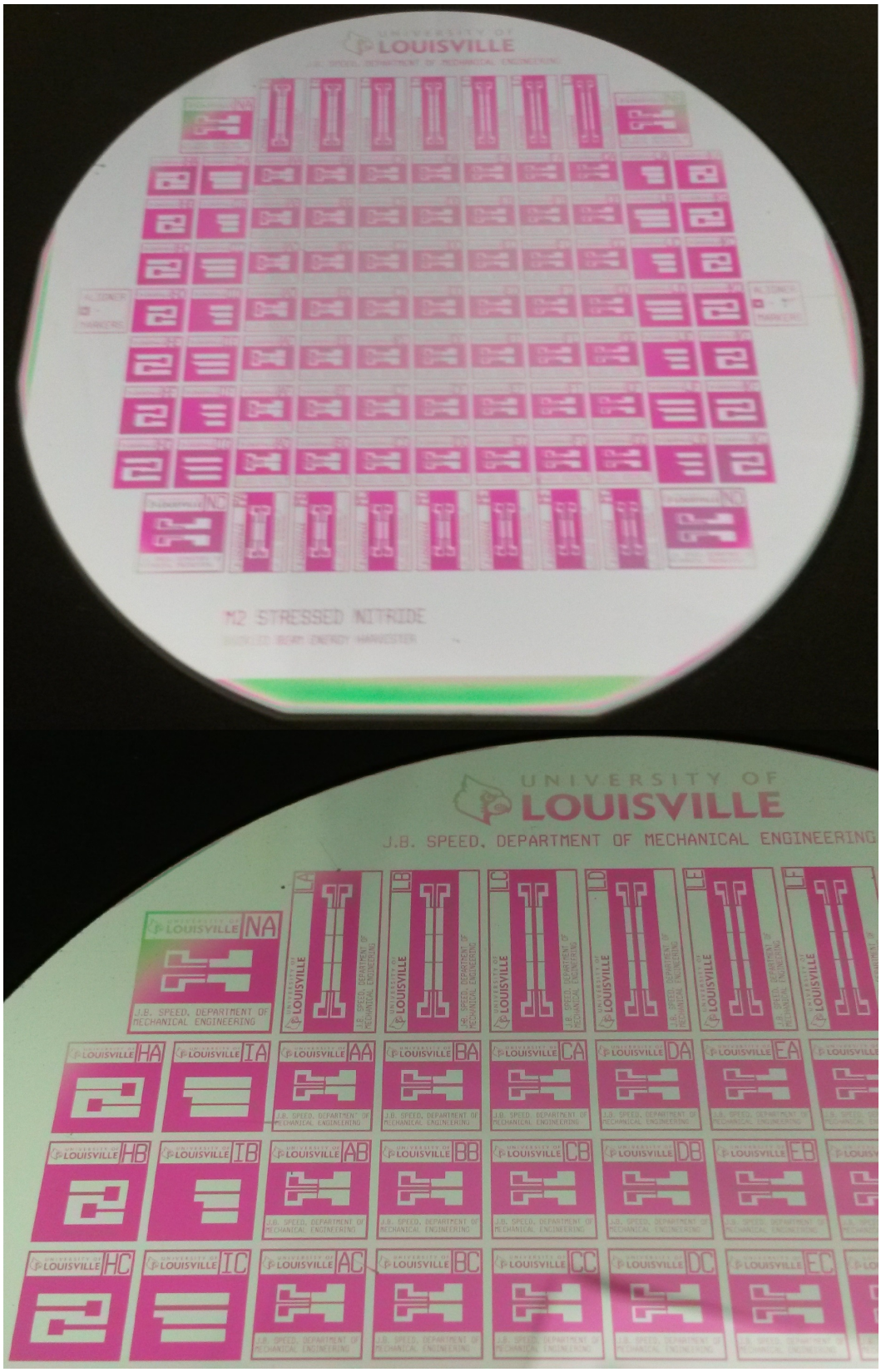

FIGURE 25: Processing photos following steps 6 and 7: patterning the front side stressed nitride layer with a BSA of the stressed nitride mask and etching the excess material.

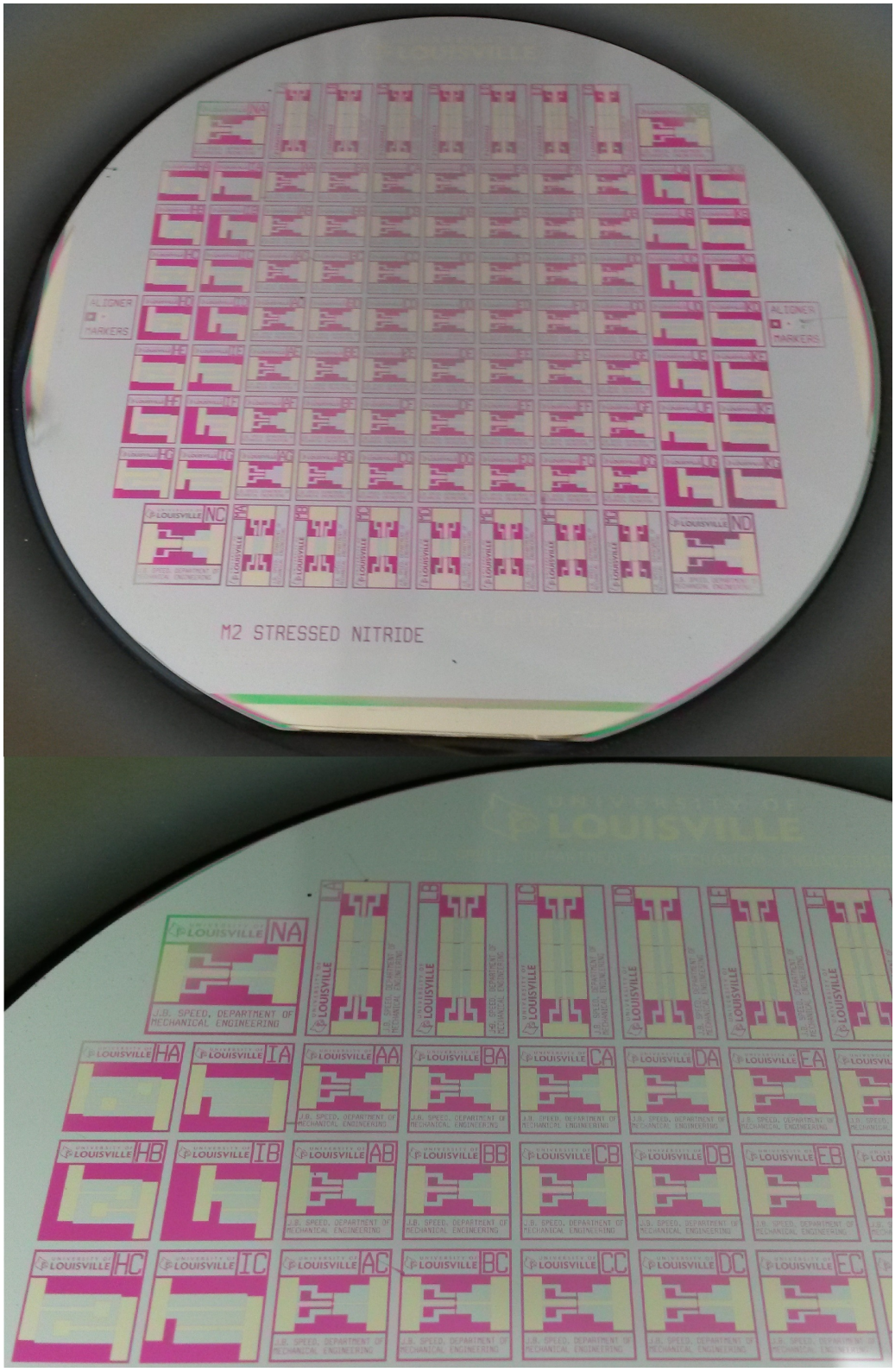

FIGURE 26: Processing photos following steps 8 to 10: deposit, pattern, and etch a molybdenum material layer corresponding to the bottom electrode mask.

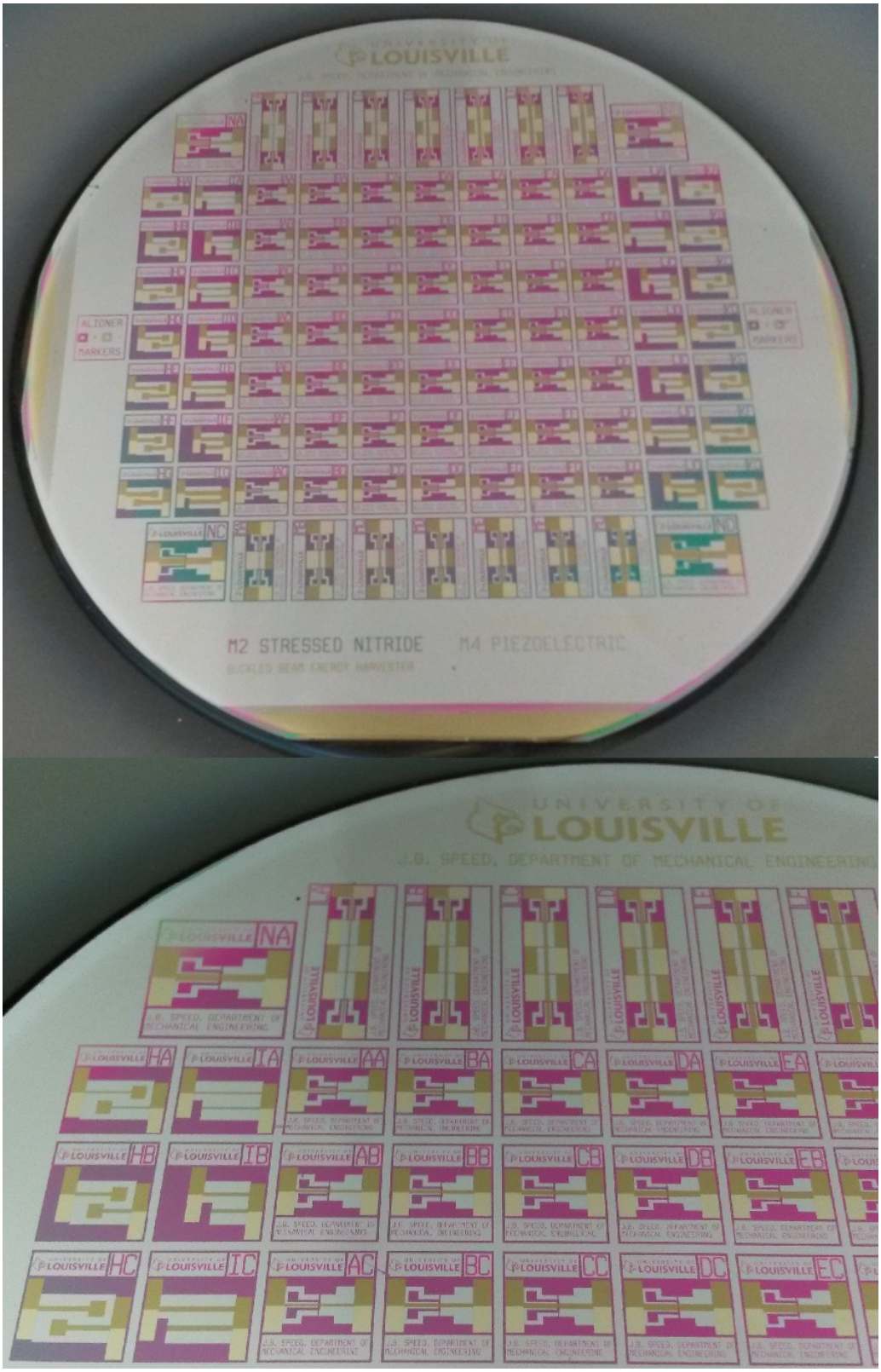

FIGURE 27: Processing photos following steps 11 to 13: deposit, pattern, and etch the piezoelectric material layer (in this case, AlN) according to the piezoelectric layer mask.

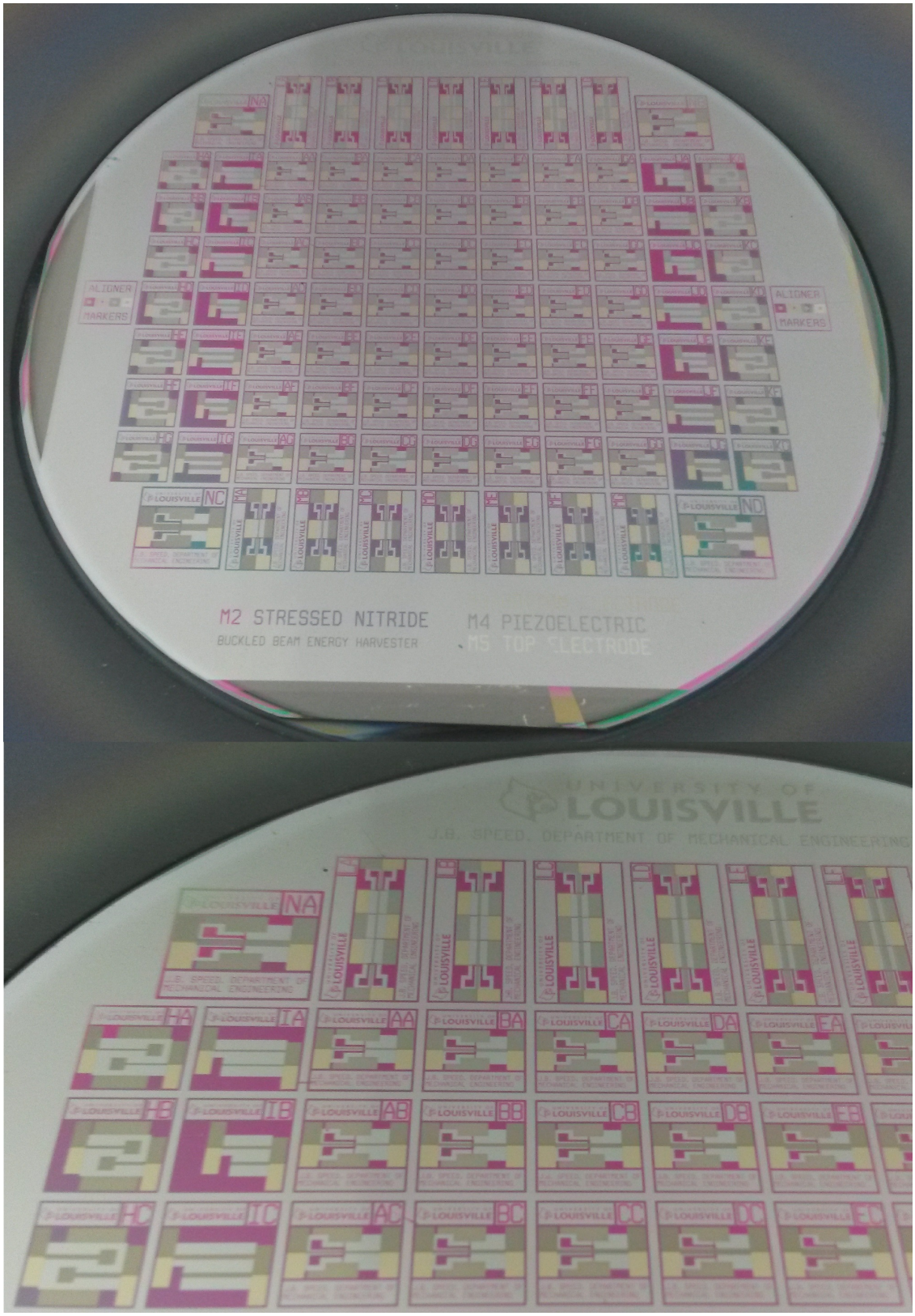

FIGURE 28: Processing photo following steps 14 to 16: deposit, pattern, and etch a second molybdenum layer according to the top electrode mask.

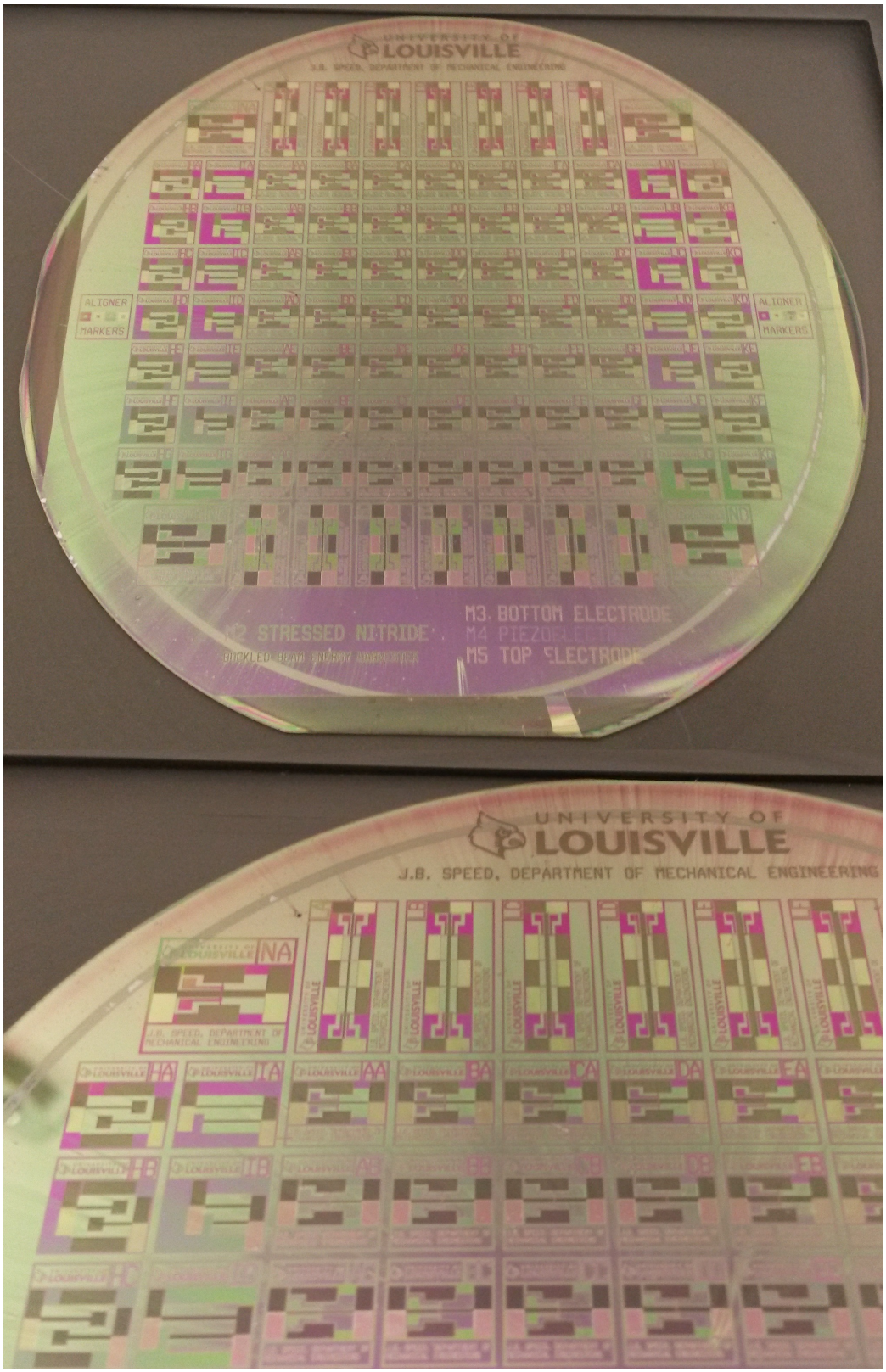

FIGURE 29: Processing photo following step 17: deposit a protective photoresist layer on top side of processed wafer.

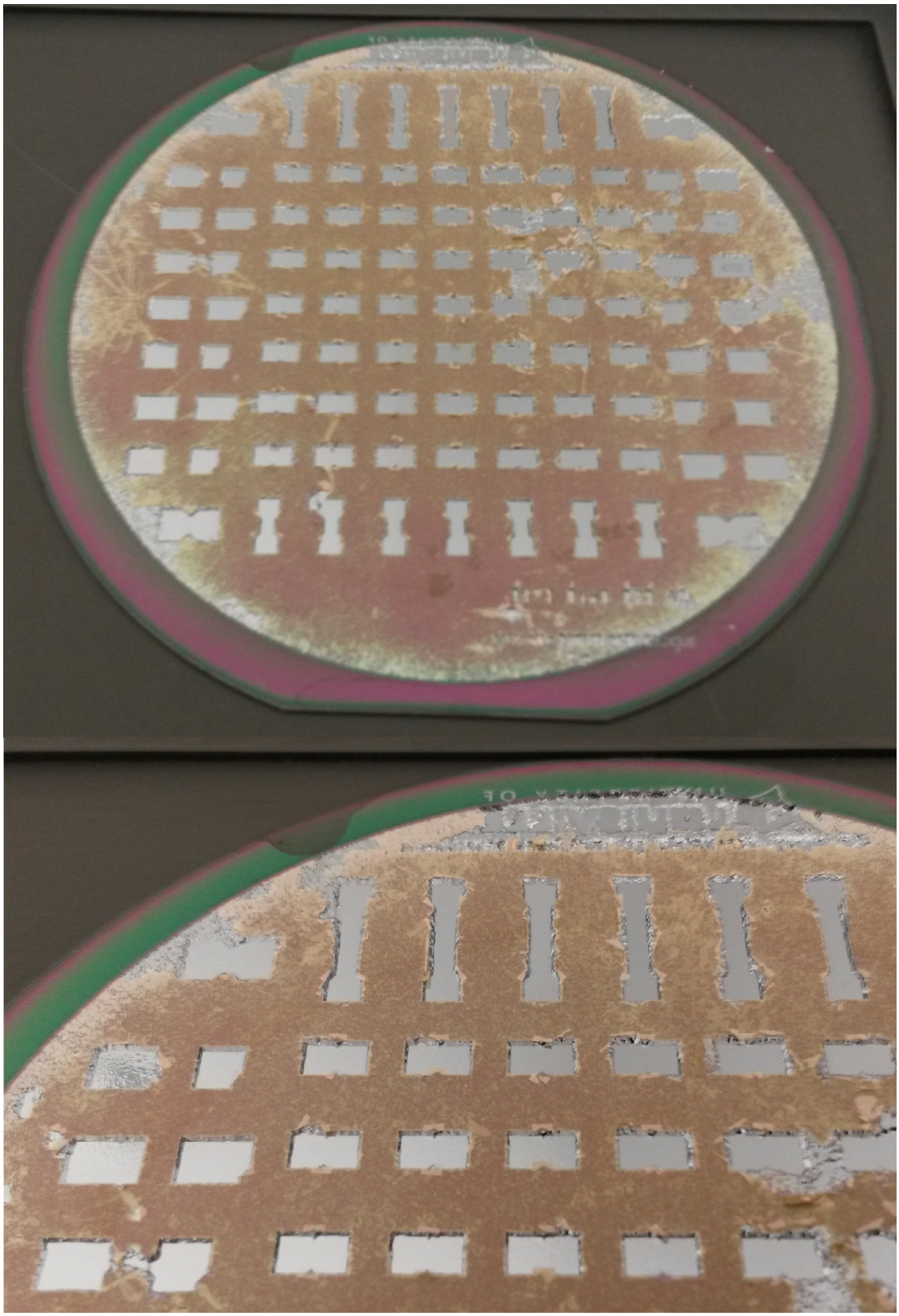

FIGURE 30: Processing photo following steps 18 and 19: perform BOE (if it were necessary) and a KOH bulk etching bath for 4 hours and 20 minutes exactly.

FIGURE 31: Processing photo following step 20: dice the wafer (performed by MNTC staff) into individual device cells.

V. RESULTS AND FURTHER ANALYSIS

A. Issues in Prototype Fabrication

As is often the case with experimental research, the attempted fabrication of a prototype device was not without its many issues and complications. While the research of this text resulted in great strides toward a functional prototype, such a device was unable to be fully fabricated in the single year of research time allotted. This section illustrates the several major problems associated with the device fabrication; some potential solutions are provided, while other issues remain inhibitors to further progress within the current state of the research.

KOH Etching

The majority of problems associated with the device fabrication involve the final release phase of the process flow, which begins with a lengthy KOH etching step. There are several issues corresponding to KOH etching, although the success of the etching has increased dramatically over the course of this research.

Firstly, over-etching is perhaps the most likely cause of a failed etch. If a sample wafer remains in the KOH bath for too long, the cells will become extremely thin and may burst. The substrate window thickness at which this occurs has been observed to be as large as $20 - 30$ μm. The exact mechanism which causes this cell bursting is unknown, whether that be due to fluid pressure or turbulent movement within the bath, small imperfections within the substrate, or simply the violent and forceful nature of the chemical reactions taking place. Regardless, once even a single cell has

burst while submerged in the KOH bath, the processed side of the wafer (normally protected via the wafer fixture) becomes exposed to the wet etchant and is immediately destroyed (at least in terms of any energy harvesting capabilities). Figure 32 displays one of many examples of a processed wafer with many ruptured cells (this image also perhaps displays evidence of a depth-dependent etching rate gradient of the KOH bath).

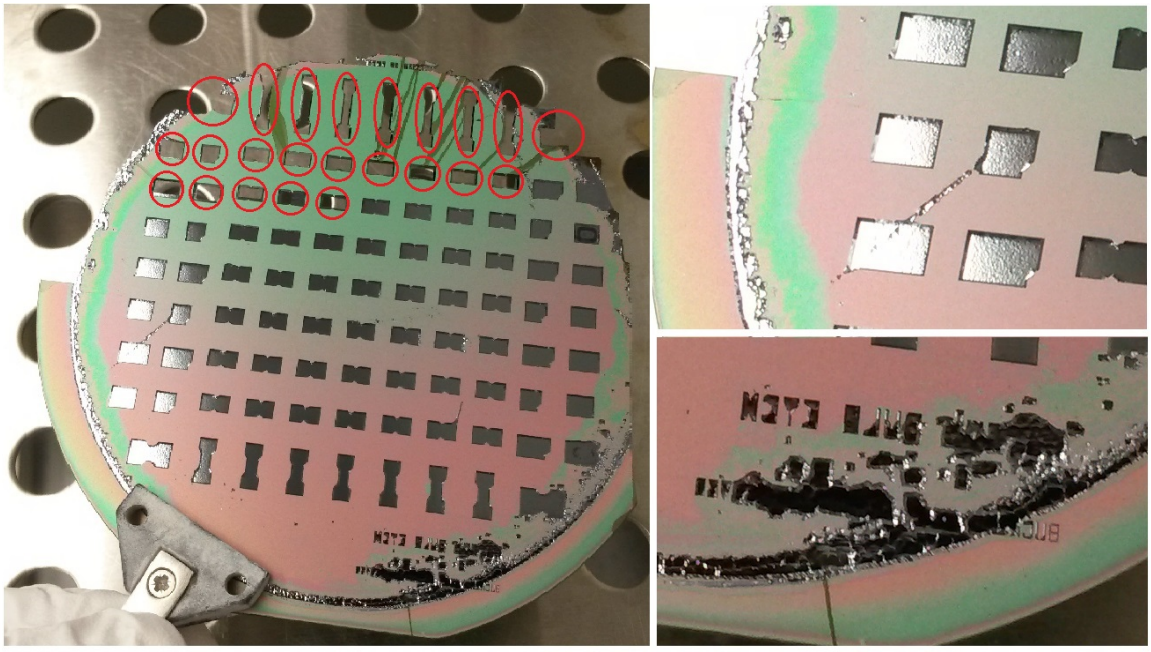

FIGURE 32: Examples of the destructive chemical forces of the KOH solution. The majority of the cells in the top three rows of the wafer (left) have been completely destroyed (red ovals), exposing the top side of the processed wafer to the etchant. Imperfections in the nitride film are greatly amplified (top right), and the patterned text is entirely destroyed (bottom right).

It seems the only true solution to this issue is experimental measurement of etching rates and careful timing of the etching process. Even a minute longer than the desired length of etching is enough to jeopardize the rigidity of the cell structures. For 380 μm wafers, an etching of 4 hours 20 minutes is used to create windows to a depth of about 350 μm. For thin 200 μm wafers, a period of 2 hours 5 minutes is used for windows roughly 170 μm deep.

Secondly, it is highly possible for the KOH solution to leak into the wafer fixture

(Figure 33) and ruin the unexposed side of the processed wafer. This issue is especially likely if the wafer fixture utilizes used or old O-rings. It is recommended that these O-rings be replaced before every etch and that they are seated firmly and properly within the fixture before encasing the processed wafer. The fixture should then slowly be tightened (via a typical star pattern tightening technique) until there is no visible gap or crack between the fixture body and top cover.

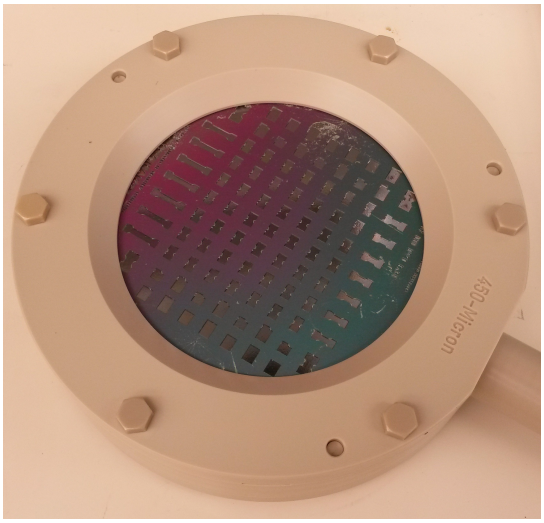

FIGURE 33: The wafer fixture used to expose only the patterned back side of the wafer to the KOH etchant while protecting the processed top side.

Thirdly, KOH etching in general causes deterioration of convex corners within a masking window, as predicted by the simulation shown in Figure 21. In fact, the convex corner over-etching observed during experimentation was even more severe that that displayed in the simulation, as illustrated in Figure 34. This rather unexpected phenomenon leads to virtually no substrate support for the anchoring nitride arms on either side of the main device beam at the top side of the wafer. This undoubtedly severely decreases the integrity of the device. Unfortunately, convex corner deterioration is an unavoidable consequence of KOH etching. Perhaps the best workaround solution to this issue is a redesign of the backside window photomask which utilizes oversized support structures that will be etched down to a more appropriate and effective size.

Device Release

In addition to KOH wet etching, a final dry etching release step is required to free each cell structure. This process too contains issues which are in need of resolution.

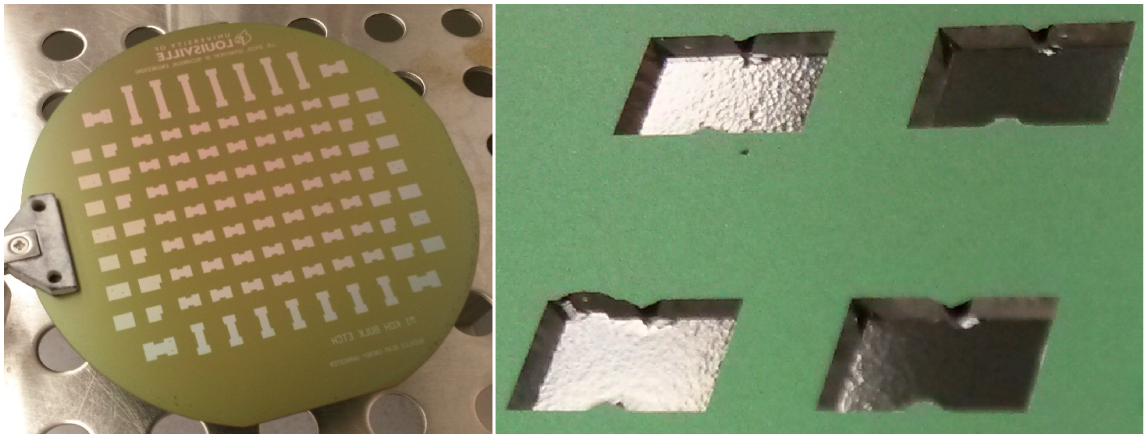

FIGURE 34: The rather unexpected and severe convex corner etching (right) caused by the KOH solution, as compared to the expected general window shapes before etching began (left). This corner deterioration significantly reduces the substrate support for the anchoring nitride arms placed on either side of the central beam node.

Most importantly, each device's patterned thin films seem to burst as soon as the supporting substrate begins to vanish. Ideally, a successful device fabrication would result in a freestanding structure without the need for any underlying substrate support at all. This phenomenon is most likely intimately tied with the issue of the device's inherent stress and apparent fragility (discussed in further detail within the next subsection). Figure 35 displays several examples of ruptured cells after slow and careful dry etching of the remaining substrate.

While the previously-described final release method utilizes gas compositions of CHF_3 and SF_6, another substrate etching method could prove to be more effective. In this alternate method, xenon difluoride (XeF_2) is employed to etch the silicon substrate while maintaining a very high selectivity with respect to the other materials (meanwhle, the previous recipe etched nitride at a fairly non-trivial rate). Perhaps the different chemistry and greater selectivity will allow for more controlled, consistent, and selective release of the final structure.

However, the bursting of the device cells may also be evidence of a lack of supporting nitride and piezoelectric material film thicknesses (also discussed in the following subsections). Figure 36 displays close-up images of a pair of simple beam and can-

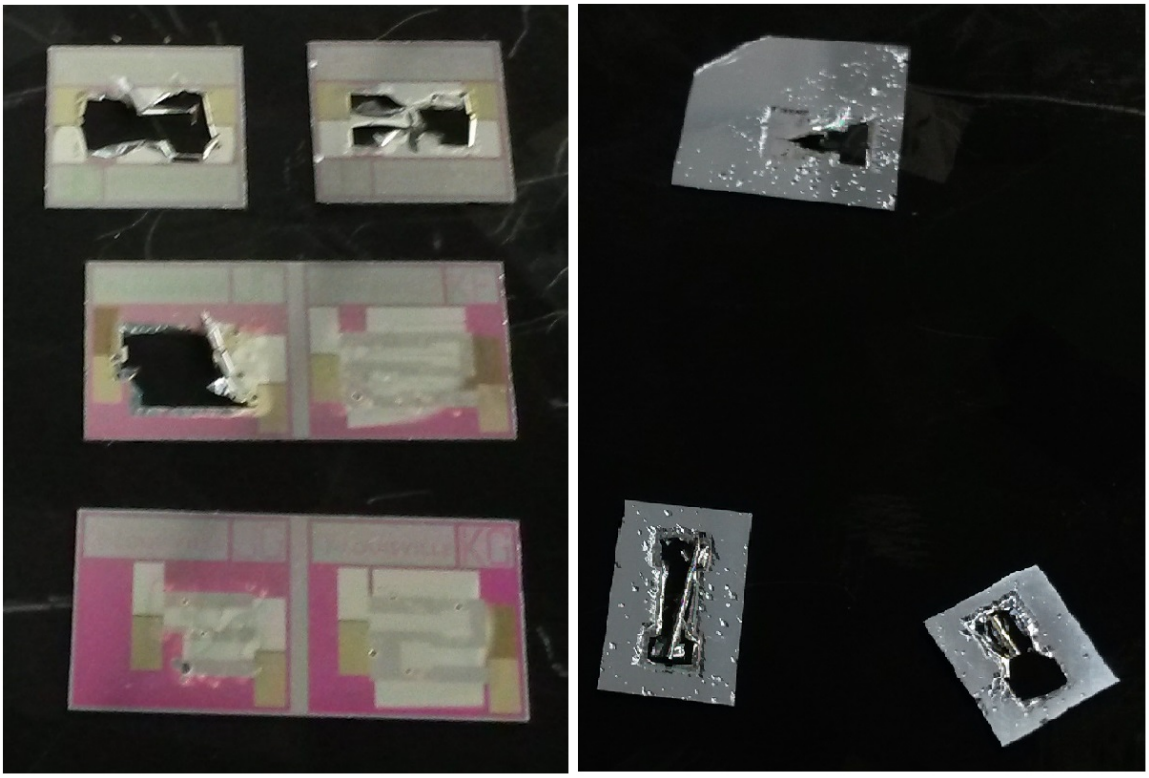

FIGURE 35: Several different device cells (including single- and dual-node harvester cells, a large-scale single-node cell, and multiple simple beam and cantilever pairs of cells) are ruptured as the supporting substrate is etched away.

tilever cells. The left image displays the cells barely held together via an extremely thin film (less than a few μm) of silicon substrate. However, it is important to note that neither the nitride nor the piezoelectric material layers are visible in this image; this is inferred from the gap in structural material seen in the beam cell. Such a gap is present only in the electrode geometries used to pattern the material layers, but not within the nitride and piezoelectric layer geometries.

In the right image of Figure 36, the simple beam cell has ruptured completely (after roughly a minute of further substrate etching). Meanwhile, the cantilever device layers have begun to peel away with the remaining remnants of silicon substrate within the cell window. Indeed, if any device lacks a significant layer of structural nitride or piezoelectric material, then there is no hope of the device surviving a complete release step since the electrodes alone do not provide sufficient structural geometry.

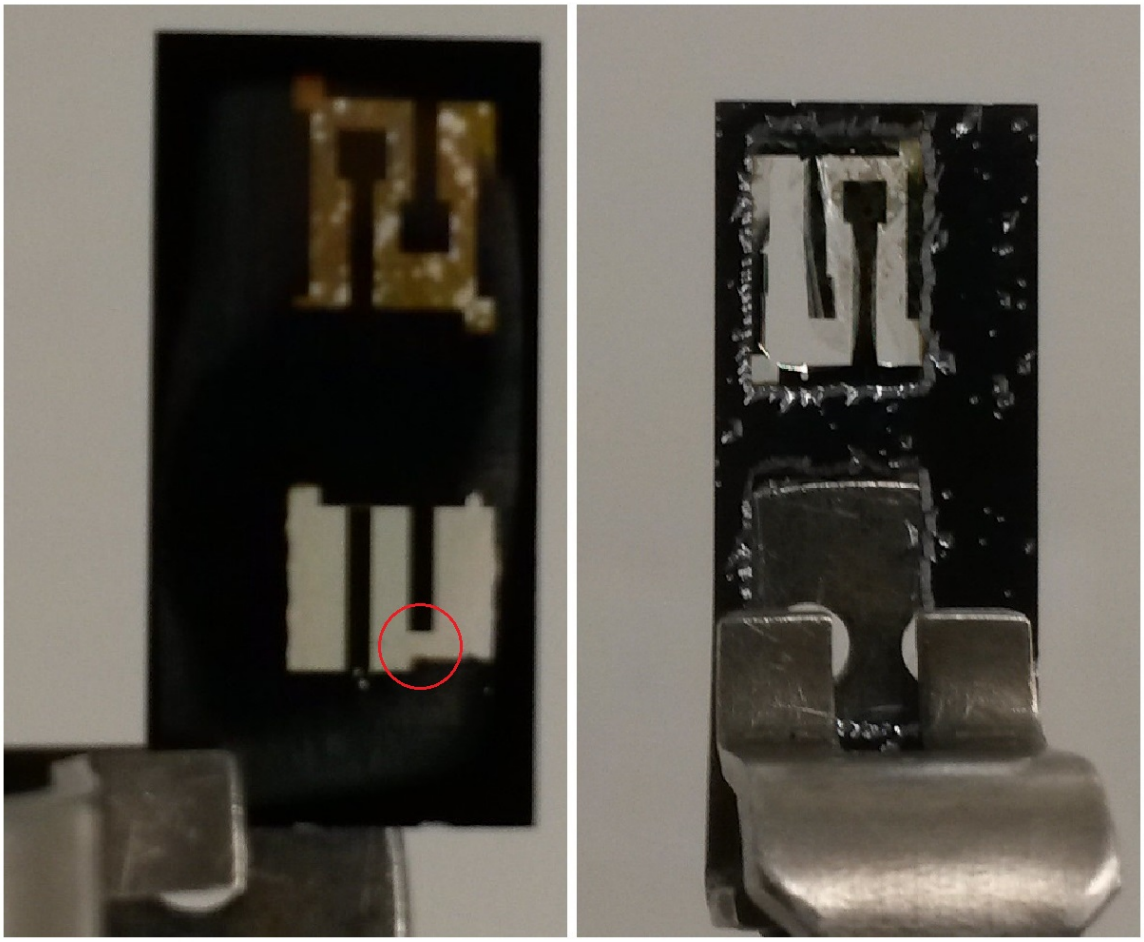

FIGURE 36: A pair of simple beam and cantilever cells (left, top side) remain intact via an extremely thin film of substrate which remains after several periods of dry silicon etching. It is observed that the opaque structural material of the simple beams consist of only the patterned electrode layers and not the nitride or piezoelectric layers. Unfortunately, the simple beam cell ruptures completely after seconds of additional etching (right, back side), while the cantilever beams begin to peel away from thin substrate fragments remaining within the cell.

There are several possible reasons why these important structural layers are not observed during the final release etching step. Firstly, it is possible that the layers of silicon nitride and aluminum nitride are simply not as reflective as, say, molybdenum electrodes and thus are not nearly as visible (if at all) when viewed solely as extremely thin freestanding films. Similarly, the thin silicon substrate films within the original cells of Figure 36 are virtually invisible but are indeed present nonetheless.

It is also somewhat possible that these nitride and piezoelectric layers are unknowingly etched away at some point in the microfabrication process. However, this seems

unlikely since the only times within the fabrication process during which this could occur is during the removal of the patterned photoresist after etching the excess material (steps 7 and 13) or actually during the final silicon etching (step 21). However, it seems that the corresponding fabrication example images (Figures 25 and 27) clearly display a newly added, patterned material to the wafer for both cases of the silicon nitride and aluminum nitride. Additionally, it seems quite unlikely that either of the two structural layers could be etched during the final silicon substrate etching, since Figure 36 was taken when a thin layer of substrate remained, thus allowing access to the nitride and piezoelectric layers impossible from the back side of the wafer.

Given the above arguments and assuming that the silicon nitride and aluminum nitride thin films are indeed present within the devices of Figure 36 and other similarly processed cells, one can conclude that these two structural materials—as they are created via the depositions described previously in this text—are insufficient for providing the structural rigidity needed for the device to be self-supportive. Specific issues surrounding these materials, especially those related to this general insufficiency, are discussed in the following subsections.

Stress and Fragility

The PECVD silicon nitride layer forms the foundation for the proposed device's geometry and is the driving structure behind the device's buckling characteristics. As such, the nitride layer plays a crucial role in the rigidity of any properly freed devices and also in the failure of any ruptured cells.

Perhaps most importantly, the inherent compressive stresses of the nitride layer (in tandem with the stresses of the remaining layers) could be great enough to tear the device apart as soon as the supporting substrate is etched away to some critical thickness or if the nitride becomes delaminated from the substrate surface. The stresses typically observed via the recipe of this text are on the order of -400 MPa

for a nitride layer thickness of roughly 560 nm.

Potential solutions could be to decrease the magnitude of this stress via the controlled pulsing of RF and HF powers during the PECVD process. Figure 37 graphically displays the approximate relationship between the fraction of deposition time spent utilizing RF power and the resulting stress of the nitride film. It is inferred that a greater amount of time utilizing RF power yields less compressive internal stresses; thus, a more heavily-weighted HF deposition may result in more manageable stress levels in terms of device rigidity and rupturing.

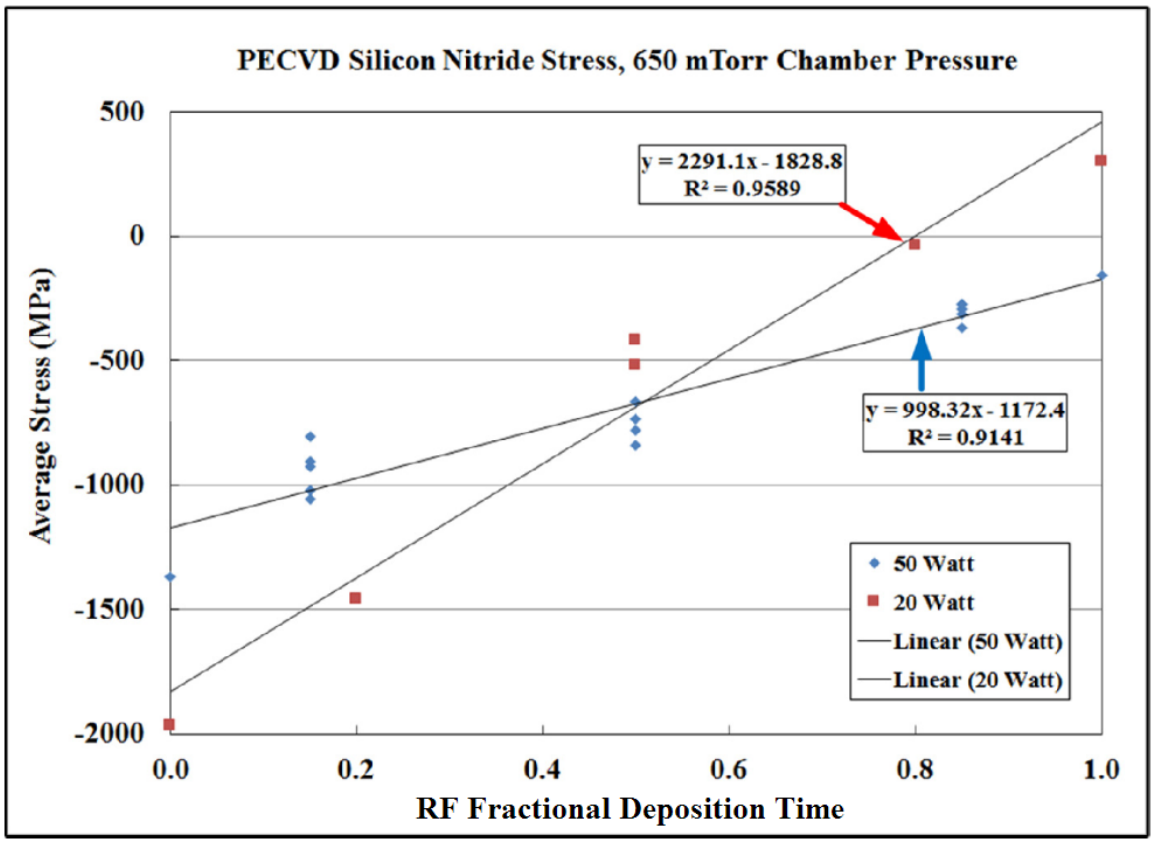

FIGURE 37: A plot (courtesy of previous graduate student of this research) displaying experimental results of the silicon nitride film's inherent stress versus the fractional amount of PECVD deposition time utilizing a RF pulse (as opposed to a HF pulse). [16]

However, the other device layers contribute a nonzero stress to the system as well. Assuming aluminum nitride has been deposited for the piezoelectric layer, a combined tensile stress on the order of 150 MPa is easily possible due to the piezoelectric stack.

This significant difference in stress states between the supporting nitride and the piezoelectric stack most likely has profound consequences regarding the profile of a released device. A stress gradient across the thickness of a film would result in a bending moment and potential failure of the film if the gradient is sufficiently substantial.

A test was performed in order to further understand the effects of large stresses within the thin films of the device. A patterned nitride layer was deposited onto a sample wafer via the *un*stressed nitride recipe. No piezoelectric stack was deposited. Instead, the ordinary release process was applied to the test wafer in order to successfully free the unstressed nitride films. Indeed, the nitride patterns in several cells were successfully freed, as shown in Figure 38. Further, the freed nitride layers were practically invisible when not held against a dark background, providing additional evidence to previous comments about the presence of the nitride within the completed samples. In conclusion, it seems stress within the device layers (especially nitride, but perhaps within the piezoelectric stack as well) is the primary cause of cell bursting.

Aside from inherent stress, the thickness of a structural film will greatly affect its strength. In order to increase the chance of processed devices surviving the final release step, the thickness of the nitride and piezoelectric films could be significantly increased. This proposal would be simple enough to carry out for the depositions of silicon nitride or PVDF; however, aluminum nitride already requires an extremely lengthy, complex, and somewhat inconsistent deposition, so the production of a significantly increased layer of AlN may prove rather difficult.

Further, an important point must be noted: while robustness of the device is highly desirable for intended usage, flexibility of the device's main beam is equally important in order to readily allow for beam buckling. Thus, an ideal balancing point between the device's strength and flexibility should be a primary goal within the continuation of this research—if such a balance is physically possible at all.

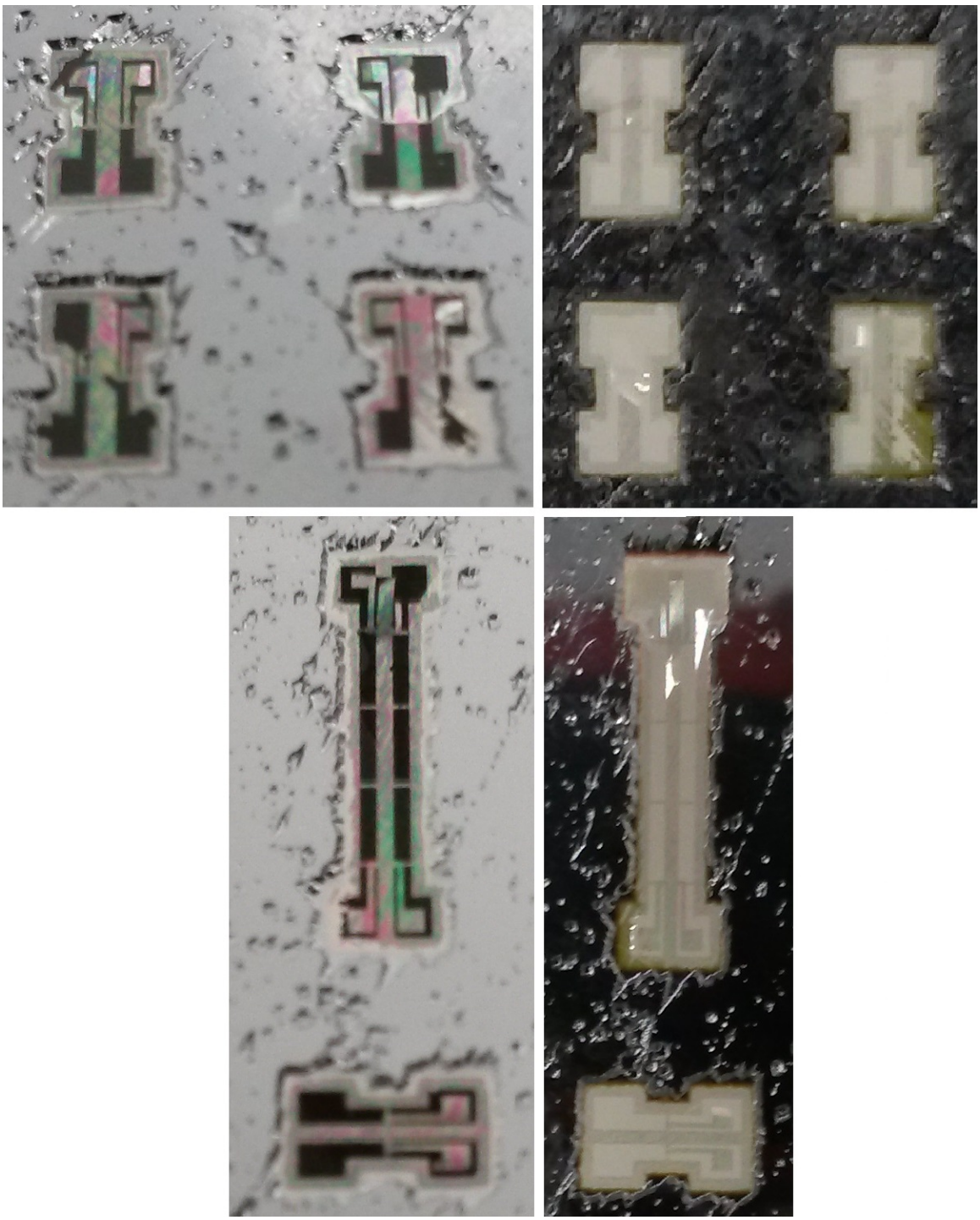

FIGURE 38: Several examples of successfully freed cells (left) consisting solely of patterned *un*stressed nitride films which have remained mostly or entirely intact during the release etching process. When these nitride films are not held against a dark background, they become nearly invisible (right) to the naked eye.

Piezoelectric Properties

While depositing materials such as aluminum nitride or PVDF may be straightforward enough in many cases, it is quite challenging to develop such a deposition procedure which actually results in materials with significant, consistent, and usable piezoelectric characteristics. Indeed, two major issues surround the piezoelectric materials described in this research: consistency of measurable piezoelectric response, and electrical shorting between the electrodes within the piezoelectric stack.

The piezoelectric response of material samples are measured via an oscilloscope with leads electrically connected to the full-wafer-wide bottom electrode and to one of multiple small circular top electrodes deposited on top of the piezoelectric material being tested. This top electrode pattern is formed via utilizing a shadow mask during the electrode deposition, as illustrated in Figure 39.

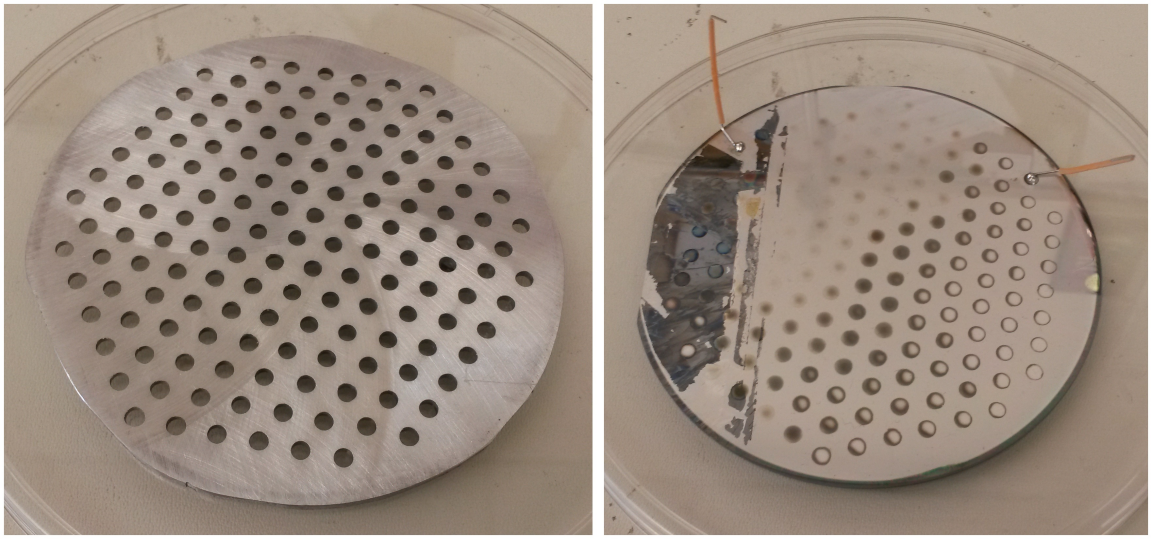

FIGURE 39: The aluminum shadow mask (left) used for depositing a top electrode pattern (right) consisting of numerous separated wiring pads for the purpose of testing unpatterned piezoelectric samples.

At first, the aluminum nitride material deposited via the heated PVD recipe given previously in the text displayed promising piezoelectric characteristics. This was inferred from the fact that the oscilloscope produced noticeable spikes when

the piezoelectric stack sample was lightly struck, inducing a small amount of strain. However, subsequent tests have been unable to repeat this result. It is not known whether the promising results of the first tests were false positives, or that later tests suffered from some unknown flaw, such as electrical shorting within the stack. Further testing will be needed to fully determine the piezoelectric properties of the aluminum nitride and to ensure experimental repeatability.

Unfortunately, the piezoelectric properties of the PVDF have yet to be tested due to repeated issues regarding electrical shorting. It seems the PVDF recipe described previously produces a quite consistently porous material. Such porosity readily leads to shorting through the material, even for the smallest diameter electrodes. A proposed solution to this issue is to employ a vacuum oven in place of a standard atmospheric pressure oven during the multiple curing phases of the PVDF process. It is thought that the lack of pressure will force the deposited material more evenly across the surface of the sample and reduce overall porosity.

Piezoelectric materials are vital to the success of the proposed harvester device. Thus, any issues concerning the fabrication and testing of these materials must be of high priority to any researcher involved in the development of a novel MEMS PEH.

B. Performance Experimentation

The primary goal of this research is to produce a device which can harvest electrical energy from ambient vibrations. To verify any success regarding this goal, the fabricated prototype device must be tested under conditions similar to those expected of application environments and the resulting performance measured and analyzed. Unfortunately, due to one or several of the reasons listed in the previous section, a prototype device has yet to be successfully and completely fabricated; thus, this performance experiment is planned to take place in the future once this research has produced a functional prototype.

However, a viable testing apparatus is currently operational within the research laboratory and is ready to undergo testing as soon as a completed device is ready. This apparatus, known as a shaker table (displayed in Figure 40), utilizes the variable-frequency displacements of a large-diameter speaker head to vibrate an elevated testing platform onto which a sample device is placed. The electrical signal to the speaker can be modified according to the desired application testing scenario. The figure illustrates a macro-scale bistable buckled beam model undergoing shaker table testing.

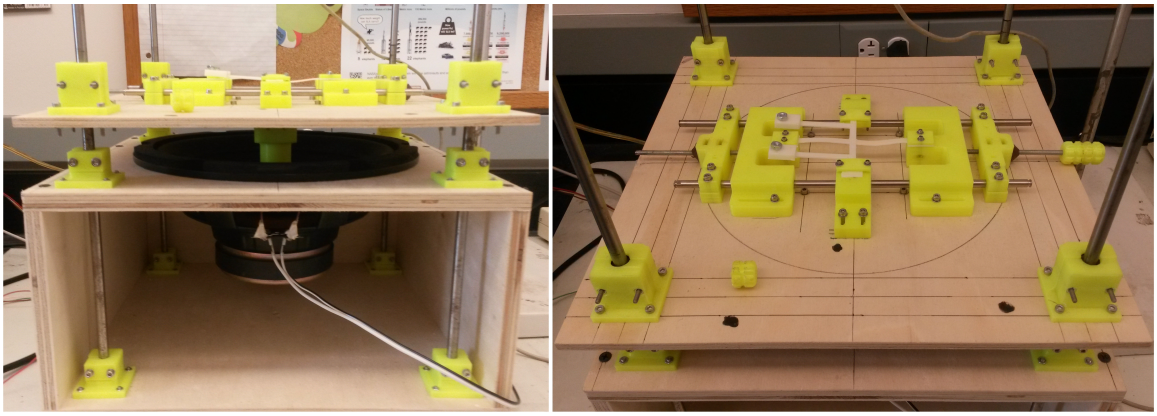

FIGURE 40: The shaker table apparatus to be used in future device performance testing. The large-diameter speaker head (left) receives signal input and displaces the top-mounted platform (right) accordingly. A macro-scale bistable buckled beam geometry is currently under testing.

Performance experimentation on a prototype MEMS PEH—especially in the case that the testing produces successful energy harvesting results—would be a great milestone achieved within this research. If a novel, nonlinear energy harvester design can be successfully demonstrated within a controlled setting, then the technology would indeed be one step closer to application within real-world environments outside of the laboratory. The next step beyond proof-of-concept demonstration is refinement of design in the hopes of maximizing efficiency, reliability, and general usefulness in terms of energy harvesting.

VI. CONCLUSIONS

A. Future Work

The research of this text has provided significant progress toward a functional prototype device of a novel MEMS PEH. Even so, continued research into the project will be necessary not only to provide a proof-of-concept device, but to expand on an original prototype in order to continually improve the device and adapt the design to best suit potential applications for the future. Utilizing the presented research provided thus far as a solid foundation, one may be hopeful that future work will provide even greater contributions to the field of microscale energy harvesting.

The most pressing issues to be resolved in the coming research are those presented in the previous chapter. Most notably, it is likely that the presented process flow and/or corresponding fabrication recipes will need to be slightly modified in order to consistently yield structurally stable devices. As previously concluded, it is likely that a combination of reducing the magnitude of the inherent compressive stresses within the nitride layer and increasing the film thicknesses of the nitride and piezoelectric materials will greatly increase the stability of the resulting device structures.

Once such a fabrication process has been established, the piezoelectric properties of the device must be explored further. While the aluminum nitride has produced promising signs in past experimentation, further study is needed to quantify and confirm these results, especially within the context of a completed microscale device. Further, at least minor changes must be made to the current PVDF recipe in order to produce films with greater thickness consistency and significantly less porosity. Once

these materials have been proven to maintain piezoelectric properties, a virtually endless amount of effort could be put forth into refining the deposition recipes in order to maximize the produced piezoelectric effects.

In order to test the quality and effectiveness of the piezoelectric material in question—and the completed device as a whole—a shaker table will be employed, as described in the previous chapter. Adequate experimentation should provide evidence of the device's electrical response characteristics as they correspond to various input frequencies, amplitudes, and waveform variations. It is desired that the device provides significant electrical response over a wide range of excitation frequencies, comparable or greater than the output corresponding to other nonlinear devices, such as that illustrated in Figure 5. The goal of this research is to be produce a novel, nonlinear energy harvester design which utilizes a bistable, buckled beam geometry to provide significant electrical output in response to a wider range of input characteristics than can be achieved via more traditional, linear harvester designs; it is within this experimental testing phase when the success (or lack thereof) of the research will be most fully determined, and the need for any subsequent changes to the device design or fabrication process revealed.

Further, any successfully fabricated device must be adequately packaged before it is even feasibly ready for a true application environment. Device packaging is highly important as it provides both the protection which the fragile structures need from the surroundings, as well as the electrical interconnectivity which allows the device to be readily applied in conjunction will other electrical devices (such as wireless transceivers). Connectivity from the device's electrode pads to the packaging requires precise wire bonding techniques. Past experimentation with molybdenum electrodes has resulted in weak and brittle bonding between the electrode and corresponding testing wires. Thus, research into alternative device electrode materials and/or various electrical bonding substances (such as silver epoxy) may prove worthwhile.

B. Concluding Remarks

In summary, the past year of graduate research—culminating in the text of this thesis writing—has provided a fairly small yet somewhat significant contribution to the microscale energy harvesting scientific research community. While the rather short timeline of this research opportunity has proven insufficient to complete all intended goals, the progress that has indeed been made provides a firm foundation for future research to continue and to reach these goals within the context of MEMS piezoelectric energy harvesters.

While traditional harvesters rely on linear mechanics and thus are fairly insufficient at providing largely applicable harvesting capabilities over a broad range of input frequencies, nonlinear devices have been proven to be significantly more responsive. The nonlinear, bistable buckled beam energy harvester design proposed in this thesis fills the gap between the more efficient harvesting mechanics of nonlinear systems and the microscale size regime of modern electronics. Such a device can be easily envisaged as a power source in low-power applications, such as wireless sensors, receivers, transmitters, among many others.

A complete design of the device was constructed in two-dimensional layout software which was used to create corresponding photomasks necessary for the microfabrication of the device in the cleanroom. In additional to the original, single-node version of the device, several variations and auxiliary devices were designed as well, including two- and four-node devices, oversized single-node devices, simple beam devices, and traditional cantilever beam devices. These layouts provide both the current microfabrication material layer patterns as well as saved software templates to be easily modified for future design iterations of the device.

Within the University of Louisville's Micro/Nano Technology Center, a great amount of fabrication experimentation was conducted over the course of the year

in order to provide the most efficient and effective process flow for fabricating a fully processed wafer of devices. Detailed recipes for all necessary depositions, etching processes, and photolithography procedures were carefully noted. While many fabrication issues were resolved throughout the research, a few major problems remain. Further study and experimentation into the causes of these issues has yielded significant insight, and the findings and potential solutions have been provided.

Utilizing the efforts of this thesis as a foundation, future work within this research will hopefully continue to provide progressive advancements in the fabrication of the proposed piezoelectric bistable buckled beam energy harvester.

REFERENCES

[1] R. Elfrink, T. M. Kamel, M. Goedbloed, S. Matova, D. Hohlfeld, Y. van Andel, R. van Schaijk. "Vibration energy harvesting with aluminum nitride-based piezoelectric devices." *Journal of Micromechanics and Microengineering.* Aug., 2009.

[2] N. G. Stephen, "On energy harvesting from ambient vibration," *Journal of Sound and Vibration* 293, pp. 409-425, 2006.

[3] J. M. Renno, M. F. Daqaq, D. J. Inman, "On the optimal energy harvesting from a vibration source," *Journal of Sound and Vibration* 320, pp. 386-405, 2009.

[4] S. Roundy, "On the effectiveness of vibration-based energy harvesting," *Journal of Intelligent Material Systems and Structures* vol. 16, pp. 809-823, 2005.

[5] I. L. Guy, S. Muensit, E. M. Goldys, "Extensional piezoelectric coefficients of gallium nitride and aluminum nitride," *Applied Physics Letters* vol. 75, no. 26, pp. 4133-4135, 1999.

[6] B. H. Hwang, C. S. Chen, H. Y. Lu, T. C. Hsu, "Growth mechanism of reactively sputtered aluminum nitride thin films," *Material Science and Engineering* 325, pp. 380-388, 2002.

[7] N. Cohen, I. Bucher, "On the dynamics and optimization of a non-smooth bistable oscillator – Application to energy harvesting," *Journal of Sound and Vibration* 333, pp. 4653-4667, 2014.

[8] M. Vangbo, "An analytical analysis of a compressed bistable bucked beam," *Sensors and Actuators* 69, pp. 212-216, 1998.

[9] F. Maurin, A. Spadoni, "Wave dispersion in periodic post-buckled structures," *Journal of Sound and Vibration* 333, pp. 4562-4578, 2014.

[10] I. D. Breslavsky, M. Amabili, M. Legrand, "Nonlinear vibrations of thin hyperelastic plates," *Journal of Sound and Vibration* 333, pp. 4668-4681, 2014.

[11] S. P. Beeby, M. J. Tudor, N. M. White, "Energy harvesting vibration sources for microsystems applications," *Measurement Science and Technology* 17, pp. 175-195, 2006.

[12] J. T. Lin, K. Walsh, B. Alphenaar, "Enhanced stochastic, subharmonic, and ultraharmonic energy harvesting," *Journal of Intelligent Material Systems and Structures* 24 (11), pp. 1324-1331, 2012.

[13] W. Q. Liu, A. Badel, F. Formosa, Y. P. Wu, A. Agbossou, "Novel piezoelectric bistable oscillator architecture for wideband vibration energy harvesting," *Smart Materials and Structures* 22 (11), 2013.

[14] University of Louisville, *Micro/Nano Technology Center.* April, 2017. Website, "www.louisville.edu/micronano."

[15] A. Toprak, O. Tigli, "MEMS scale PVDF-TrFE-based piezoelectric energy harvesters," *Journal of Microelectromechanical Systems* 24 (6), pp. 1989-1997, 2015.

[16] D. A. Porter, T. A. Berfield, "A bi-stable buckled energy harvesting device actuated via torque arms," Ph.D. dissertation, Department of Mechanical Engineering, University of Louisville, Louisville, KY, 2014.

CURRICULUM VITA

NAME: Brian Edward Allgeier

ADDRESS: 9909 Tunnel Way
Louisville, KY 40291

DOB: June 2, 1994 (Louisville, KY)

EDUCATION: B.S. Physics and Astronomy
University of Kentucky
2012-2016

B.S. Mathematics
University of Kentucky
2012-2016